

## On the energy conversion characteristics of a top-mounted pitching absorber by using smoothed particle hydrodynamics

Zheng, Xiaobo; Chen, Guangmao; Cao, Wenjin; Xu, Hao; Zhao, Ruiwen; Xu, Qianlong; Kramer, Morten; Touzé, David Le; Borthwick, Alistair G.L.; Li, Ye

*Published in:*  
Energy Conversion and Management

*DOI (link to publication from Publisher):*  
[10.1016/j.enconman.2021.114893](https://doi.org/10.1016/j.enconman.2021.114893)

*Creative Commons License*  
CC BY-NC-ND 4.0

*Publication date:*  
2021

*Document Version*  
Accepted author manuscript, peer reviewed version

[Link to publication from Aalborg University](#)

*Citation for published version (APA):*  
Zheng, X., Chen, G., Cao, W., Xu, H., Zhao, R., Xu, Q., Kramer, M., Touzé, D. L., Borthwick, A. G. L., & Li, Y. (2021). On the energy conversion characteristics of a top-mounted pitching absorber by using smoothed particle hydrodynamics. *Energy Conversion and Management*, 250, Article 114893. <https://doi.org/10.1016/j.enconman.2021.114893>

### General rights

Copyright and moral rights for the publications made accessible in the public portal are retained by the authors and/or other copyright owners and it is a condition of accessing publications that users recognise and abide by the legal requirements associated with these rights.

- Users may download and print one copy of any publication from the public portal for the purpose of private study or research.
- You may not further distribute the material or use it for any profit-making activity or commercial gain
- You may freely distribute the URL identifying the publication in the public portal -

### Take down policy

If you believe that this document breaches copyright please contact us at [vbn@aub.aau.dk](mailto:vbn@aub.aau.dk) providing details, and we will remove access to the work immediately and investigate your claim.



# On the energy conversion characteristics of a top-mounted pitching absorber by using smoothed particle hydrodynamics

Xiaobo Zheng<sup>a</sup>, Guangmao Chen<sup>a</sup>, Wenjin Cao<sup>a</sup>, Hao Xu<sup>a,b</sup>, Ruiwen Zhao<sup>a</sup>,  
Qianlong Xu<sup>a</sup>, Morten Kramer<sup>c</sup>, David Le Touzé<sup>d</sup>, Alistair G.L. Borthwick<sup>e,f</sup>, Ye  
Li<sup>a,b,g,\*</sup>

<sup>a</sup>*Lab of Multiple Function Towing Tank, School of Naval Architecture, Ocean & Civil Engineering,  
Shanghai Jiao Tong University (SJTU), Shanghai, China*

<sup>b</sup>*State Key Lab of Ocean Engineering, SJTU, Shanghai, China*

<sup>c</sup>*Department of the Built Environment, Aalborg University, Aalborg, Denmark*

<sup>d</sup>*LHEEA Lab, Ecole Centrale Nantes and CNRS, Nantes, France*

<sup>e</sup>*School of Engineering, The University of Edinburgh, Edinburgh, UK*

<sup>f</sup>*School of Engineering, Computing and Mathematics, University of Plymouth, Plymouth, UK*

<sup>g</sup>*Key Lab of Hydrodynamics (Ministry of Education), SJTU, Shanghai, China*

---

## Abstract

The top-mounted pitching point absorber is one of the most promising wave energy converters in that it can be easily attached to an existing offshore structure. However, it is difficult to predict accurately its energy conversion performance because of the strongly nonlinear hydrodynamic behaviour. Herein, smoothed particle hydrodynamics (SPH) is used to solve this wave-structure interaction problem. The SPH method is first validated against free surface deformation measurements obtained from a wedge water entry experiment. SPH simulations of regular wave interaction with fixed and freely pitching devices agree well with measured data, providing confidence in the prediction of power conversion performance. Absorbed power and capture width ratio exhibit uni-modal behaviour with wave period. The wave period of peak power within this distribution increases with PTO damping. According to the observed scaling behaviour with device scale, an optimally damped larger scale device is effective at absorbing energy from incident waves of longer wavelength. In finite deep water, the larger device achieves higher efficiency compared with the smaller ones, and its peak efficiency at  $2\pi h/\lambda = 1.1$  provides reference for siting.

**Keywords:** wave energy conversion, top-mounted pitching point absorber, smoothed particle hydrodynamics, capture width ratio, scale effect

---

\*Corresponding Author: ye.li@sjtu.edu.cn

---

## **Nomenclature**

### **Abbreviations**

2D two dimensions

3D three dimensions

c-Si PV crystalline silicon photovoltaic cell

CFD computational fluid dynamics

CFL Courant-Friedrichs-Lewy

CWR capture width ratio

NS Navier-Stokes

P1, P2, P3, P4, P5 elevation probe in wave tank

PTO power take-off system

RANS Reynolds-Averaged-Navier-Stokes

RNG renormalised group

RP reference point of wedge-water entry

SPH smoothed particle hydrodynamics

VoF volume of fluid

WEC wave energy converter

### **Operators**

$\bar{\phantom{x}}$  mean value

$\sigma(\phantom{x})$  standard deviation value

$\vec{\nabla}$  gradient vector

$||$  magnitude value

## Symbols

$\alpha$	non-dimensional dissipation coefficient in artificial viscosity term
$\alpha_D$	coefficient in smoothing function
$\delta$	coefficient of density diffusion term
$\epsilon_x, \epsilon_z$	relative coordinate discrepancies, %
$\gamma$	coefficient in Poisson's equation
$\Pi$	artificial viscosity term
$\lambda$	wave length, m
$\lambda_I$	wave length in water of infinite depth, m
$\mu$	intermediate variable in artificial viscosity term
$\rho$	fluid density, kg/m <sup>3</sup>
$\rho_0$	reference fluid density, kg/m <sup>3</sup>
$\vec{F}_d$	damping force on PTO, N
$\vec{F}_e$	excitation force on PTO, N
$\vec{g}$	acceleration of gravity, m/s <sup>2</sup>
$\vec{r}$	displacement vector between any two given particles
$\vec{v}_r$	relative velocity of PTO, m/s
$\vec{v}$	particle velocity, m/s
$B$	intermediate variable in Poisson's equation
$C$	linear damping coefficient, Ns/m
$c$	local sound speed, m/s
$c_0$	sound speed in water of reference density $\rho_0$ , m/s
$D$	diameter of absorber hemispherical bottom, m

$F_x, F_z$	load components on the float, N
$Fr$	Froude number
$H$	wave height, m
$h$	water depth of wave tank, m
$H_d$	wedge drop height, m
$l$	smoothing length
$M$	PTO mass, kg
$m$	particle mass, kg
$P$	absorbed power, w
$p$	pressure, Pa
$P_w$	incident power in regular waves, w
$q$	non-dimensional distance between two particles
$Re$	Reynolds number
$T$	wave period, s
$t$	time, s
$W$	smoothing function of SPH interpolation
$x, y, z$	spatial coordinate
$X_c$	translation of disabled PTO cylinder, m
$Z_s$	free surface elevation, m

### **Subscripts**

$i$	the calculated particle
$j$	a neighbouring particle
$n$	index of time step
$o$	optimal damping condition
$th$	theoretical variable

## 1. Introduction

Ocean wave energy, an abundant, locally concentrated form of marine renewable energy [1], has received much attention because of its potential benefits for global energy security and environmental protection. Falcão [2] has provided a comprehensive review of different wave energy conversion technologies. According to energy conversion principles, main wave energy converters (WECs) can be classified as overtopping systems [3, 4], oscillating bodies [5, 6], oscillating water columns [7, 8], and membrane devices [9, 10].

### 1.1. Challenge of wave energy

Over the past few decades, WEC technology has evolved from prototype design towards pilot demonstration devices at ocean test sites. For example, Wave Dragon deployed the world's first offshore grid-connected WEC, an overtopping system, in 2003 [3]. Ocean Power Technologies deployed a 150 kW floating point absorber in 2011 [6]. Oceanlinx deployed a 1/3 scale demonstration device of an oscillating water column in 2010, the tests indicating that a full scale OWC could achieve a rated power of 2.5 MW [8]. Despite their successful operation, these technologies have not yet reached commercialisation because of issues concerning reliability and cost compared with other renewable power sources [11], such as offshore and onshore wind, crystalline-silicon photo voltaic (c-Si PV) and hydro-power (figure 1).

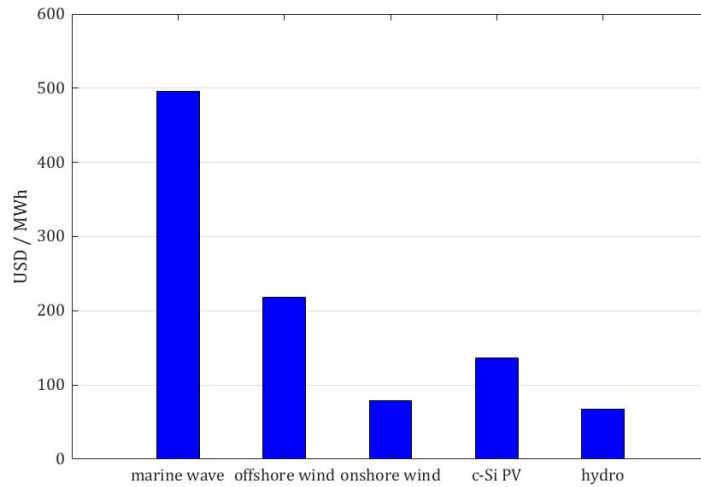


Figure 1: Global levelised cost of renewable energy technologies in 2013 (figure by permission of the World Energy Council, London [12]).

Of all the foregoing challenges, cost is the most important, and is mainly affected by energy conversion efficiency and device scale [13, 14]. Theoretically, the conversion efficiency from energetic waves per unit volume (usually characterised by capture width ratio, CWR) is relatively limited [15, 16]. Much research effort on WEC is therefore directed towards improving conversion efficiency and hence reducing energy cost. The floating point absorber, a form of oscillating body WEC, is believed to be one of the most cost-efficient technology by which to extract wave energy [10, 17]. Further to the absorber oscillating in heave, the concept of a pitching point absorber involves mounting an arm on the top of the absorber with a single pitching degree of freedom.

### 1.2. Top-mounted pitching point absorber

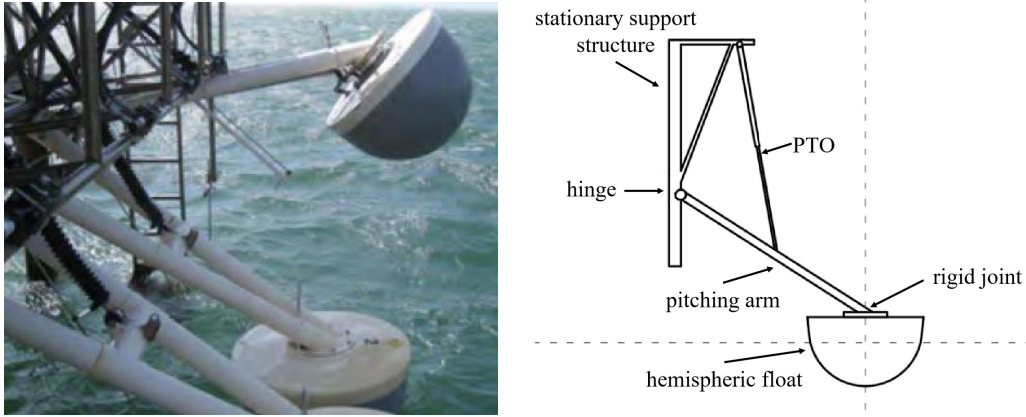


Figure 2: Left: photograph of a Wavestar device deployed at Nissum Bredning, Denmark [18]; right: general concept of top-mounted pitching point absorber.

The top-mounted pitching point absorber is designed to work together with other technologies on an offshore platform [19, 20, 21]. In this way, construction, deployment, and maintenance costs can be substantially reduced, and so such absorbers offer great potential for deep ocean applications. Perhaps the best known top-mounted pitching point absorber supplying electricity to the grid is Wavestar [22], which was first proposed by Niles and Keld Hansen in 2000 [23]. In Wavestar, several hemispherical-bottomed floats are connected to a stationary support structure with rigid arms. Each arm is attached at a fixed angle to the top of the float by a rigid joint. Float motion is constrained to a single rotational degree of freedom about the hinge point between the stationary support structure and the arm. Wave power is transformed into mechanical motion of the float and arm, and the power driving this



motion is absorbed by means of a hydraulic power take-off system (PTO) connected to an electrical generator that delivers electrical power to the grid. Fig.2 shows a commercial Wavestar device and the general concept of a top-mounted pitching point absorber.

### 1.3. Numerical studies on the characteristics of point absorbers

In order to improve the efficiency of point absorbers, it is necessary to optimise their hydrodynamic design in the context of wave-structure interaction. Jakobsen et al. [18, 24] carried out experimental studies on top-mounted pitching point absorbers with different float sizes in a wave basin. Jakobsen et al. measured wave and motion induced loads on the absorbers in order to estimate their mean absorbed power, and provided a detailed discussion of the reliability and accuracy of the experiments. Besides experimental tests, numerical studies have proved popular for solving wave-structure interaction problems due to their relatively low cost and accessibility. Li & Yu produced a detailed review of numerical methods for modelling floating-point absorbers [10], including linear potential, empirical prediction, boundary integral equation, and Navier-Stokes (NS) equation methods.

Numerical models based on linear potential theory assume inherently that the fluid is inviscid and incompressible, the flow is irrotational, and the amplitudes of wave and device motion are small compared with the device size. Penalba et al. [25] studied the effect of the nonlinear Froude-Krylov force on spherical and cylindrical point absorbers. Jin et al. [26] investigated the effect of nonlinear viscosity on the hydrodynamics of a 1/50 scale point absorber in heave motion. However, actual wave energy devices rarely run under the small-amplitude waves in power absorption mode, for reasons of efficiency. Furthermore, sea wave conditions are ever changing, and strongly nonlinear phenomena such as slamming, crushing, and green water inundation may occur during extreme wave events [27, 28]. Linear potential flow theory performs poorly when applied to such problems [29].

Computational fluid dynamics (CFD) based on the NS equations has been widely used to study the hydrodynamics of WECs, which are influenced by strongly nonlinear free surface deformation, viscosity, turbulence, and sometimes air compressibility. Yu & Li [30] simulated a two-body floating-point absorber in heave by using the Reynolds-Averaged-Navier-Stokes (RANS) - based finite volume method with the volume of fluid (VoF) interface capture scheme and a  $k - \omega$  Shear Stress Transport turbulence model. They analysed the hydrodynamic response and energy conversion in regular waves, and demonstrated the significance of the nonlinear effects for the power output in the case of heaving point absorber under large steepness waves. Ransley et al. [31] reviewed existing CFD simulations in which the motion of a

moving structure is calculated by considering fluid-structure interaction, and then developed a fully nonlinear and coupled tool using the RANS-VoF method and the renormalised group (RNG)  $k - \epsilon$  turbulence model. They simulated hydrodynamics of the 1/10 scale Wavestar device in regular waves of varied steepness, and found the numerical results compare well with measurements by Jakobsen et al. [24]. The RANS models in the Eulerian framework require high resolution meshes. To resolve wave-structure interaction at high accuracy, Eulerian methods also need an additional interface precise capturing scheme. Furthermore, strongly nonlinear wave phenomena, such as slamming, crushing, and green water inundation, commonly occur at the free surface. When there is an additional fluid-structure interaction with a floating device, modelling of such nonlinear processes requires mesh reconstructions that can handle grid distortion, making the computation even more complicated [32, 33]. Conversely, Lagrangian particle methods are meshless, which is a key feature in the cases where the free-surface experiences large deformation. Among the Lagrangian particle methods, smoothed particle hydrodynamics (SPH) has become the most popular.

Since its original development by Gingold & Monaghan [34] and Lucy [35] in 1977 for applications in astrophysics, SPH has proved applicable to a wide range of fluid flow problems including, e.g., gas bubble dynamics [36], water wave generation and propagation [37], and fluid-structure interaction [38, 39, 40, 41, 42]. Shadloo et al. [43] reviewed applications of the SPH method in engineering fields, such as aerospace, transportation, environment, geophysics, and energy production. They summarised the motivations behind utilising the SPH method in an industrial context, and derived general conclusions regarding its assets and limitations. Compared with mesh-based Eulerian methods, SPH modelling uses interpolation functions to calculate spatial quantities and their derivatives from an arbitrary set of calculation points, giving it the meshless nature. This method naturally incorporates discontinuities across the interface and singular forces into the numerical scheme, and does not need special treatment to detect the free surface and different phases in space [33]. It also preserves perfectly sharp interfaces between phases, even in case of large deformation of the free surface or air entrapment in the water. Finally, it directly models moving complex interfaces and boundaries due to its Lagrangian nature, giving remarkable advantages regarding free surface flow simulation and wave-structure interaction analysis. Therefore, for wave energy utilisation, SPH serves as a promising tool to capture the violent hydrodynamics of waves that break, run up, overtop and interact with WECs, see, e.g., [44, 45, 46, 47, 48].

#### 115 1.4. *Research Objectives*

116 In order to balance the power capture efficiency, cost, and security of top-mounted  
117 pitching point absorbers, a deep understanding is required of the characteristics of  
118 energy conversion and associated hydrodynamics. Without loss of generality, we  
119 apply the geometry of Wavestar to study energy conversion performance by alter-  
120 ing the incident wave condition and PTO damping coefficients. Particular attention  
121 is given to the effect of float scale on absorbed power by optimised PTO. In this  
122 study, the SPH method is used to solve the wave-structure interaction problem be-  
123 cause of its inherent accuracy in capturing violent free surface deformation. More  
124 specifically, Section 2 outlines the numerical model based on the SPH method, fol-  
125 lowed by validation of its capability to accurately capture complex free surface flow.  
126 Section 3 compares the hydrodynamics of the wave-device interactions simulated by  
127 the SPH method with experimental data and alternative RANS predictions. Section  
128 4 discusses the effects of wave height, wave period, PTO damping coefficient, and  
129 device scale on absorbed power and capture width ratio. Section 5 examines opti-  
130 mal absorbed power by considering the effects of scale and water depth. Section 6  
131 summarizes the main conclusions.

## 132 2. Numerical method

### 133 2.1. *SPH method*

134 In SPH modelling, the fluid domain volume is discretised into a set of elementary  
135 fluid volumes called particles. Spatial differential operators involved in the evolu-  
136 tion equations of the system, e.g. the Navier-Stokes equations, are computed by  
137 interpolation from neighbouring particles within a characteristic distance called the  
138 smoothing length. The contribution of these neighbour particles depends on the  
139 distance between particles and a weighted kernel function of compact support. The  
140 main steps of an SPH algorithm are as follows [49]: i) neighbouring particles are first  
141 searched using a linked-list algorithm [50] (for efficiency this list can be kept for a  
142 number of time steps using a slightly larger neighbourhood); ii) governing equations  
143 and boundary conditions are then solved with involved spatial differential operators  
144 estimated through the aforementioned interpolation; iii) particle quantities are up-  
145 dated using standard or symplectic time integration schemes. In the present work,  
146 a standard weakly compressible SPH model is used to solve the fully coupled prob-  
147 lem of wave-WEC interactions with the open source software package DualSPHysics  
148 (<https://dual.sphysics.org>).

149 The weighted kernel function of the aforementioned SPH interpolation, also called  
150 smoothing function, is noted by  $W$ . In the present work a quintic spline [51] is used

151 which can be written as a function of the non-dimensional distance  $q$  as [52, 53]:

$$W(q) = \alpha_D \left(1 - \frac{q}{2}\right)^4 (2q + 1), 0 \leq q \leq 2, \quad (1)$$

152 where  $\alpha_D$  is  $7/4\pi l^2$  in two dimensions (2D) and  $21/16\pi l^3$  in three dimensions (3D).  
 153  $q = |\vec{r}|/l$ , where  $\vec{r}$  is the displacement vector between any two given particles and  
 154  $l$  the smoothing length. The SPH method used herein assumes the fluid is weakly  
 155 compressible. Pressure is calculated from the equation of state, which is more efficient  
 156 and easier for parallel computing than by Poisson's equation [54]:

$$p = B \left[ \left( \frac{\rho}{\rho_0} \right)^\gamma - 1 \right], \quad (2)$$

157 where  $p$  is pressure,  $\rho$  is fluid density,  $\gamma = 7$ , and  $B = c_0^2 \rho_0 / \gamma$ . Another essential  
 158 feature of the weakly-compressible version of SPH compared to the incompressible  
 159 version is that no free-surface detection is needed to impose free-surface boundary  
 160 conditions in case of single-phase free-surface simulation [55, 56].  $c(\rho) = \sqrt{\partial p / \partial \rho}$   
 161 is the local sound speed, and  $c_0 = c(\rho_0)$  is the speed of sound in water of reference  
 162 density  $\rho_0$ . For computational efficiency, under the weak-compressibility assumption  
 163 an artificially low value is used for  $c_0$  so that fluid compressibility is limited to within  
 164 1% about the reference density  $\rho_0 = 1000 \text{ kg/m}^3$  for water.

165 In the used DualSPHysics package the discrete SPH continuity and momentum  
 166 equations are expressed as [53]:

$$\frac{d\rho_i}{dt} = \sum_j m_j \vec{v}_{ij} \cdot \vec{\nabla}_i W_{ij} + 2\delta l c_0 \sum_j (\rho_j - \rho_i) \frac{\vec{r}_{ij} \cdot \vec{\nabla}_i W_{ij}}{|\vec{r}_{ij}|^2} \frac{m_j}{\rho_j}, \quad (3)$$

167 and

$$\frac{d\vec{v}_i}{dt} = - \sum_j m_j \left( \frac{p_j + p_i}{\rho_j \rho_i} + \Pi_{ij} \right) \vec{\nabla}_i W_{ij} + \vec{g}_i, \quad (4)$$

168 where  $m$  is particle mass,  $\vec{v}$  is particle velocity, and  $\vec{g}$  is acceleration of gravity.  
 169 Subscripts  $i$  and  $j$  indicate the calculated particle and a neighbouring particle re-  
 170 spectively, thus  $\vec{v}_{ij} = \vec{v}_i - \vec{v}_j$  and  $\vec{r}_{ij} = \vec{r}_i - \vec{r}_j$ . In standard (fully-Lagrangian) SPH  
 171 simulations, the mass of each fluid particle remains constant so that the density can  
 172 be not explicitly involved in the first term on the right side of the continuity equation  
 173 [52]. In addition, following Molteni & Colagrossi [57] a density diffusion term with  
 174  $\delta = 0.1$  is added in the continuity equation to reduce density fluctuations in the sim-  
 175 ulations. Note that more sophisticated form of this density diffusion term was later

176 proposed by Antuono et al. [58]. In the momentum equation, the symmetric form of  
 177 plus pressure discretization [59] is utilised for the conservation of linear and angular  
 178 momenta in the particle system. Considering the required accuracy [37, 40, 45] and  
 179 computational costs, the simple artificial viscosity model is adopted in the momen-  
 180 tum equation instead of other more accurate models [60]. The common form of the  
 181 artificial viscosity term  $\Pi$  is written as,

$$\Pi_{ij} = \begin{cases} -\frac{\alpha \bar{c}_{ij} \mu_{ij}}{\bar{\rho}_{ij}}, & \vec{v}_{ij} \vec{r}_{ij} \leq 0, \\ 0, & \vec{v}_{ij} \vec{r}_{ij} > 0, \end{cases} \quad (5)$$

182 where  $\mu_{ij} = l \vec{v}_{ij} \vec{r}_{ij} / (r_{ij}^2 + 0.01 l^2)$ ,  $\bar{c}_{ij} = (c_i + c_j)/2$ , and  $\bar{\rho}_{ij} = (\rho_i + \rho_j)/2$ .  $\alpha$  is the  
 183 non-dimensional dissipation coefficient with a positive value, which is chosen as small  
 184 as possible to avoid excessive dissipation for violent-dynamic flows. In the present  
 185 study,  $\alpha = 0.01$  is found to be a good choice to avoid excessive dissipation [37] and  
 186 to improve the numerical stability [39]. Note that since no physical viscosity term  
 187 is discretized and the artificial viscosity term tends to zero with particle refinement,  
 188 the momentum equation is essentially an Euler equation, which is an appropriate  
 189 choice for the targeted application.

190 A numerically stable explicit second-order symplectic method is used as the time  
 191 integration scheme. This method is with a time accuracy of  $O(\Delta t^2)$  and involves  
 192 predictor and corrector stages. A variable time step criterion [61] is used within the  
 193 time integration, i.e., the time step is dependent on the Courant-Friedrichs-Lewy  
 194 (CFL) condition, the mass force term and the viscous diffusion term. The speed  
 195 of sound, mass force and viscosity force are calculated for all particles at each time  
 196 step, which in turn determines the size of the next time step with the value of the  
 197 CFL number adopted as 0.2.

198 In the present single phase SPH modelling, the free surface is identified by search-  
 199 ing for the interpolated nodal mass larger than a given reference mass which is set as  
 200 half the fluid mass in 3D [53]. The SPH model naturally incorporates discontinuities  
 201 across the interface into the numerical scheme. Therefore, no other special treatment  
 202 is needed as mesh-based Eulerian methods [33]. A shifting algorithm is used in the  
 203 DualSPHysics model. This algorithm addresses the instability issue of anisotropic  
 204 particle spacing in the violent fluid-structure-interaction cases, and eliminates noises  
 205 in the velocity, density and pressure fields caused by the instability [62].

206 Solid objects in the SPH modelling are assumed rigid. The dynamic impermeable  
 207 and free-slip boundary condition is implemented for solid boundaries of rigid objects.  
 208 In the used DualSPHysics model, the solid boundary is described as a separate set of  
 209 particles to the fluid particles. Solid boundary particles satisfy the same equations  
 210 as fluid particles. The solid objects are classified as the fixed objects (e.g. tank

211 walls and fixed float), the motion-determined object (e.g. wave maker), and the  
 212 fluid-driven objects (e.g. water-entry wedge and pitching float). These three types  
 213 of solid objects are differently treated. On the fixed objects, boundary particles  
 214 remain fixed in position. The paths of boundary particles on motion-determined  
 215 objects are calculated from an imposed motion function (Dalrymple & Knio [63]). In  
 216 contrast, the movement of boundary particles on fluid-driven rigid objects is derived  
 217 by considering the interaction with neighbouring fluid particles (Crespo et al. [64]).  
 218 If a fluid particle approaches any solid boundary and the distance between solid and  
 219 fluid particles becomes smaller than twice the smoothing length, the density of the  
 220 boundary particles becomes larger, causing a pressure increase. This results in a  
 221 repulsive force being exerted on the fluid particle due to the pressure term in the  
 222 momentum equation. The net force on each boundary particle is the summation  
 223 of the contributions from all surrounding fluid particles according to the designated  
 224 kernel function and smoothing length. The force exerted by fluids onto a solid object  
 225 is calculated as the summation of the net force of each solid boundary particle.  
 226 Furthermore, considering the calculated hydrodynamic force by fluids, the gravity  
 227 and the existing constraints, the movements of the fluid-driven object and hence of  
 228 the boundary particles are achieved by time integration [64]. The interaction between  
 229 solid objects with different restrictions (e.g., hinges and springs) is solved by using  
 230 the open source multiphysics simulation engine Project Chrono [65].

## 231 *2.2. Validation of complex free surface deformation*

232 In order to provide validation data for verifying the capability of the SPH model  
 233 to simulate violent fluid-structure interaction problems, experimental tests were car-  
 234 ried out on the entry of a 2D wedge into a tank of water. Unlike tests on a point  
 235 absorber in a water basin by Jakobsen et al. [24], which studied the loading on the  
 236 moving body, the present experiment focuses on deformation of the water free sur-  
 237 face. Simulation accuracy is then estimated by quantifying the discrepancy between  
 238 the predicted and experimental free surface deformation. SPH model performance  
 239 is checked for a series of extreme events that occur during wedge entry including  
 240 slamming, green water inundation, splashing, break-up, and recombination.

### 241 *2.2.1. Experimental setup*

242 The experiment was conducted in a water flume of length 1 m, width 0.35 m  
 243 and still water depth 1 m. The wedge was 0.3 m long, with triangular cross-section  
 244 of width 0.1 m and deadrise angle of 30 degrees. The mass of the wedge was 4 kg.  
 245 An aluminium alloy frame was use to attach the wedge. The width of the flume  
 246 and the length of the wedge had similar dimensions. In order to suppress water

247 splash from the ends of the wedge and to make the water entry an approximately 2D  
 248 phenomenon, the flume width and the wedge length were aligned by a laser aligner,  
 249 which provided a laser sheet of 2 mm thickness. To ensure single-degree-of-freedom  
 250 wedge motion in the vertical direction, two parallel vertical guide rods and four ball  
 251 bearings were used. The vertical rods were fixed to the top of the wedge, which  
 252 were also checked by the laser aligner with the direction deviation less than 3 degree.  
 253 The friction coefficient of ball bearings was 0.001, causing negligible frictions and  
 254 approximately free fall motion for the dropping wedge.

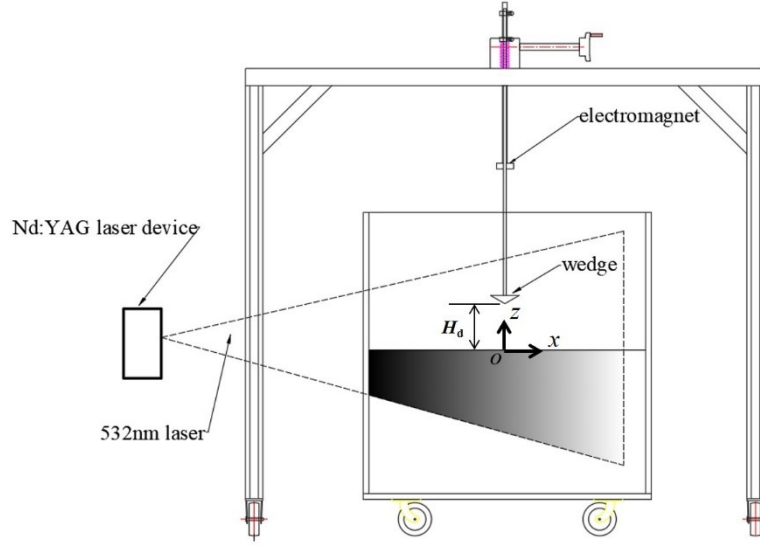


Figure 3: Schematic showing setup of 2D wedge-water entry experiment.

255 The drop height of the wedge  $H_d$  was adjusted by using a traverse system with  
 256 a resolution of 0.5 mm. The start time of the dropping was controlled by an elec-  
 257 tromagnetic switch. An Nd:YAG laser was operated in continuous mode with a  
 258 constant power output of 6 W to provide a 532 nm laser sheet. The area of in-  
 259 terest on the mid-wedge-length plane was illuminated, ensuring the 2D profiles of  
 260 free surface captured. Water entry by the wedge was monitored by a high-speed  
 261 CMOS camera, Phantom Miro eX4, with a frame rate of 1000 fps and resolution  
 262 of  $800 \times 600$  pixels. An optical filter was attached on the camera lens to suppress  
 263 image noises from external light fields. Fig.3 shows the experimental setup with the  
 264  $(x, z)$  coordinate system defined with the origin at the point of wedge entry to the  
 265 water. Here,  $x$  is in the horizontal (right positive) direction, and  $z$  is in the vertical  
 266 (upwards) direction.

### 2.2.2. Comparison between simulated and experimental results

In the experiments, the evolving interfaces between water, air, and wedge during the entry process were all captured. Fig.4 compares SPH model simulated free surface profiles (in the foreground) throughout the splash stage with experimental measurements (in the background) for cases with drop heights  $H_d = 0.05$  and  $0.10$  m at time instants  $t = 0.050$  and  $0.136$  s after the wedge first contacts the otherwise still water surface.

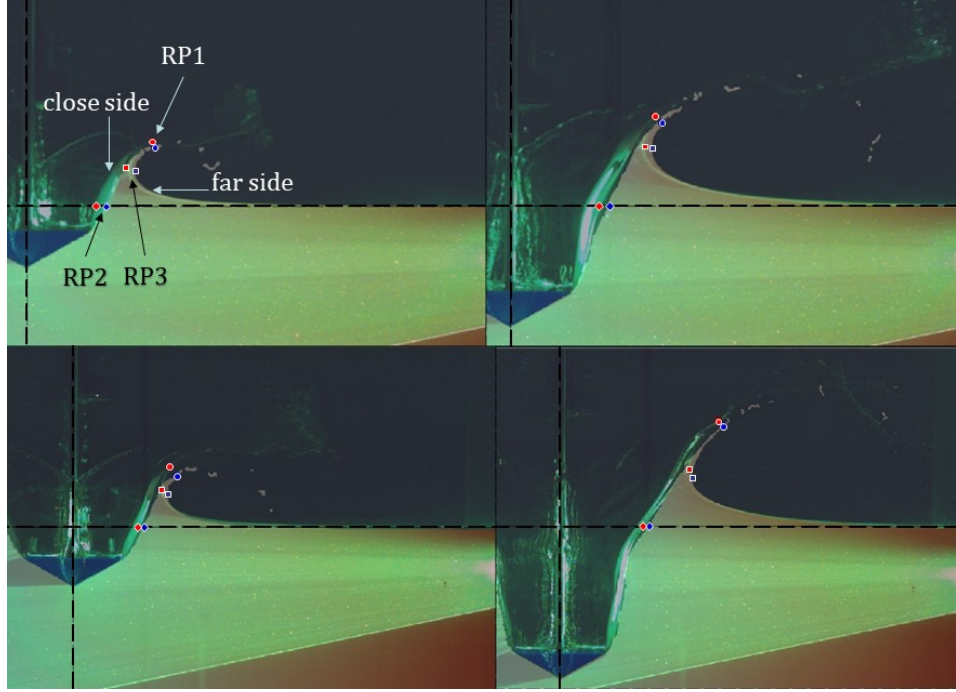


Figure 4: Comparison of free surface deformation profile and reference points (RP1: circle; RP2: square; RP3: diamond) between experiment (background contour and red symbol) and SPH simulation (foreground contour and blue symbol). Horizontal and vertical dashed lines: still water level and wedge dropping trajectory. Top:  $H_d = 0.05$  m; bottom:  $H_d = 0.10$  m. Left:  $t = 0.050$  s; right:  $t = 0.136$  s.

For  $H_d = 0.05$  m, the free surface deforms at the sides of the wedge at  $t = 0.050$  s with a plunging water jet evident. At  $t = 0.136$  s, the jet flow is more developed with an obvious increase in magnitude of free surface deformation. Compared with the free surface impacted by the wedge in the experiment, the simulated surface has less curvature and the jet splash is slightly weaker, partly because of the relatively large size of the SPH particles [41] and lack of surface tension in the theoretical model.

Both the entry velocity and slamming force increase with increased drop height.



281 Compared with the results for the  $H_d = 0.05$  m case, the free surface profile close to  
 282 the wedge for  $H_d = 0.10$  m becomes straighter and the peak of the continuous free  
 283 surface occurs further from the tip of the wedge under the larger slamming force.  
 284 Moreover, the jet splash is larger and does not collapse so quickly onto the otherwise  
 285 calm water surface. The variations in free surface deformation and jet splash due to  
 286 changing  $H_d$  are properly captured by the SPH simulation.

287 Furthermore, three reference points on the  $x - z$  plane are selected to give a quan-  
 288 titative estimate of the discrepancy between the SPH prediction and experimental  
 289 measurement. The first reference point (RP1, circle symbol) is the peak of the con-  
 290 tinuous free surface. The second one (RP2, square symbol) is at still water level (i.e.  
 291 the horizontal dashed line) on the close side. The third one (RP3, diamond symbol)  
 292 is the closest to the wedge dropping trajectory (i.e. the vertical dashed lines) on the  
 293 far side. The reference points from measurements and simulations are respectively  
 294 marked in red and blue. Here, we define the relative coordinate discrepancy  $\epsilon_x$  and  
 295  $\epsilon_z$  as the difference of the coordinate values of a simulated reference point from the  
 296 coordinate values of a corresponding measured reference point divided by the wedge  
 297 width. Table 1 lists the relative coordinate discrepancies  $\epsilon_x$  and  $\epsilon_z$  for three refer-  
 298 ence points. Although no quantitative reference could be found from other numerical  
 299 studies for comparison purposes, the present relative deviation ( $< 17\%$ ) is satisfac-  
 300 tory in terms of capturing the free surface deformation in this wedge water entry  
 301 problem. The present SPH model is therefore verified by accurately reproducing the  
 302 free surface in the violent water-structure interactions.

Table 1: Relative coordinate deviations between simulated and measured reference points.

$H_d$ , m	$t$ , s	RP1		RP2		RP3	
		$\epsilon_x$ , %	$\epsilon_z$ , %	$\epsilon_x$ , %	$\epsilon_z$ , %	$\epsilon_x$ , %	$\epsilon_z$ , %
0.05	0.050	5.0	-8.3	13.3	0	15.0	-6.7
	0.136	12.7	-12.7	16.4	0	14.5	-3.6
0.10	0.050	14.0	-16.0	12.0	0	12.0	-12.0
	0.136	8.9	-11.1	13.3	0	8.9	-15.6

### 303 3. Hydrodynamic Modelling of the scaled device

304 We now simulate the hydrodynamics of a top-mounted pitching point absorber  
 305 with a hemispherical-bottomed float in order to validate the SPH model for a more  
 306 complicated wave-structure problem.

### 3.1. Model setup

The present NWT has dimensions corresponding to the test tank considered in experimental work by Jakobsen et al. [24], as shown in the top panel of fig.5. Jakobsen et al. carried out large-scale experiments on a 1/10 scale model in the COAST Ocean Basin of the University of Plymouth, UK, and obtained measurements of wave elevation and motion-induced loads in regular waves as well as under extreme conditions. In addition, Ransley et al. [31] reproduced regular wave interactions with both a fixed and a freely-pitching 1/10 scale model using a RANS-VoF method with the RNG  $k - \epsilon$  turbulence model. With permission from Jacobsen et al., their experimental data are utilised to validate the present SPH model, and the alternative numerical results by Ransley et al. used for comparison purposes.

In the SPH simulation for validation, the computational domain is 16 m long and 6 m wide with a wave maker and a wave absorber situated at the upwave and downwave boundaries respectively. The water depth  $h$  is 3 m. The middle and lower panels of fig.5 depict the NWT and device model. The total height of the 1/10 scale float is 0.72 m, and the diameter of the hemispherical bottom is  $D = 1$  m. Below we use the hemisphere diameter  $D$  as the referential size of the scaled device. The Cartesian coordinate system is defined by the right-hand rule with the origin located at the still water surface close to the wave maker, the  $x$  ordinate directed in the horizontal wave propagation direction, and the  $z$  ordinate directed upwards in the vertical direction.

A piston type wave maker is used to produce regular long-crested waves. According to a transfer function, the displacement of the piston is calculated from the desired free surface elevation. The transfer function of a second-order Stokes theory proposed by Madsen [66] is adopted, preventing the generation of spurious secondary waves. The produced waves will not change shape as they propagate, and are absorbed by a passive damping zone with a quadratic decay function [37]. Table 2 lists the wave properties produced in the NWT, including the wave period  $T$  and the wave height  $H$ . In the SPH model, nearly 2 million particles are generated with particle size of 0.05 m. Owing to the Lagrangian nature of the SPH method and to its already mentioned property of intrinsically verifying free-surface boundary conditions, the air phase effect can be neglected and then the complex single-phase free-surface motion prediction does not require any special treatment.

The scaled device is constrained to pitch about an axis passing through the hinge point which connects the stationary support structure and the device arm. The other end of the arm is attached to the hemispherical-bottomed float. The scaled device is initially located at the neutrally-buoyant position with the hemispherical bottom centred at  $x = 5.0$  m,  $y = 0$  and  $z = 0.1$  m. The draught of the float is 0.4 m and

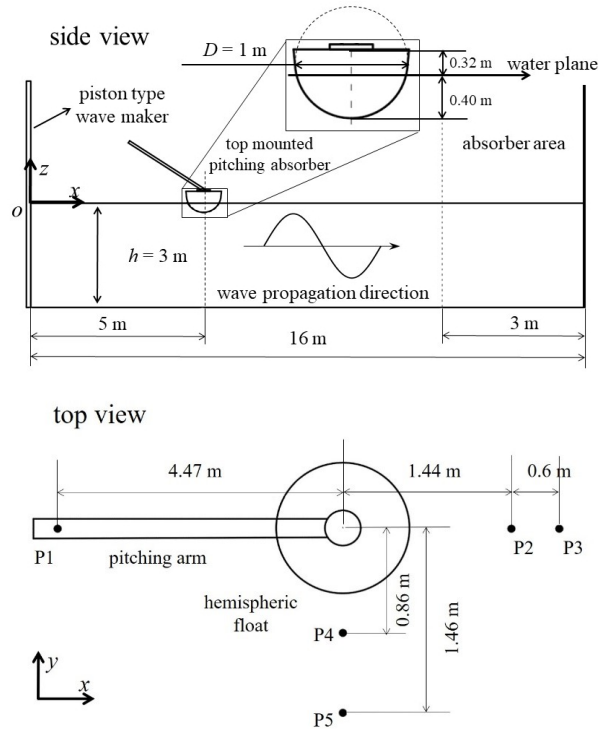
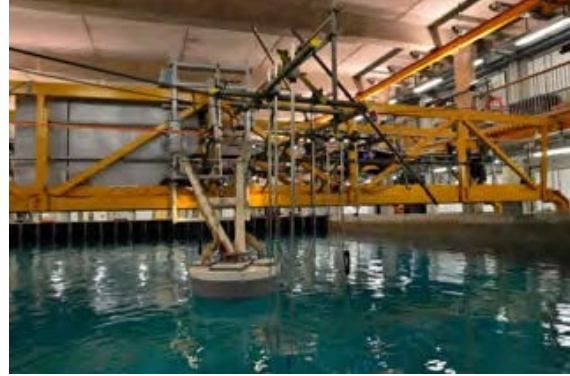


Figure 5: Top: picture of experimental setup in the Ocean Wave Basin at the University of Plymouth, UK [24]; middle: SPH numerical model of the scaled device and NWT from side view; bottom: wave probes used for surface elevation measurements for fixed device from top view.

345 the water-plane diameter is 0.98 m. The mass of the scaled device is 220 kg centred  
 346 at  $dx = 1.4$  m,  $dy = 0$  and  $dz = -1.3$  m relative to the pitching axis. The moment  
 347 of inertia for pitch motion is  $124.26 \text{ kg} \cdot \text{m}^2$ . The natural period of the model with  
 348  $D = 1$  m is about 1.9 s according to the free decay test of the present SPH simulation

Table 2: Regular wave test parameters.

	$D$ , m	$h$ , m	$T$ , s	$H$ , m	reported in
Scale 1	1	3	2.8	0.25	Section 3
	1	3	2.0	0.68	
Scale 1	1	3	1 - 6	0.25,2	Section 4
Scale 2	5	15	4 - 12	2	
Scale 3	10	30	9 - 21	2	

and the measurement by Jakobsen et al. [24].

### 3.2. Comparison with experimental results

Three cases are simulated, one for a fixed pitching scaled device, the other two for a freely pitching scaled device. We first consider regular waves with  $H = 0.25$  m and  $T = 2.8$  s, and then consider extreme waves with  $H = 0.68$  m and  $T = 2.0$  s (see table 2). In these cases, the same NWT, device geometry and initial position of the float (the neutrally-buoyant position) are considered. Note that the complexity of the simulation increases for the freely pitching device owing to the coupled motion of the float, compared with the fixed device. The complexity further increases for the extreme waves owing to the large-amplitude kinematics and strong nonlinear phenomena such as green water and slamming, compared with the small-steepness waves. However, all the execution times for hydrodynamic simulations of 18 s in three cases are about 22.5 h, running on one Intel® Core™ i7-7700HQ CPU @ 2.80 GHz processor (4 cores and 8 threads) and NVIDIA GeForce GTX 1060 GPU. In contrast, the computational cost is found to increase significantly due to the moving mesh and the large-deformation mesh in RANS-VoF simulations by Ransley et al. [31]. The limited computational cost of simulating fluid-structure-coupled kinematics and large-steepness waves is one of the advantages of the meshless SPH method over the mesh-based RANS-VoF method.

#### 3.2.1. Fixed device

In the fixed case, the model is locked at the neutrally-buoyant position throughout the simulation. Five wave probes monitor the surface elevations, as shown in the bottom panel of fig.5: P1 is positioned close to the wave maker (4.47 m upstream of the float centre), P2 and P3 are downstream of the float centre by 1.44 m and 2.04 m, and P4 and P5 are 0.86 m and 1.46 m from the float centre along the wave crest.

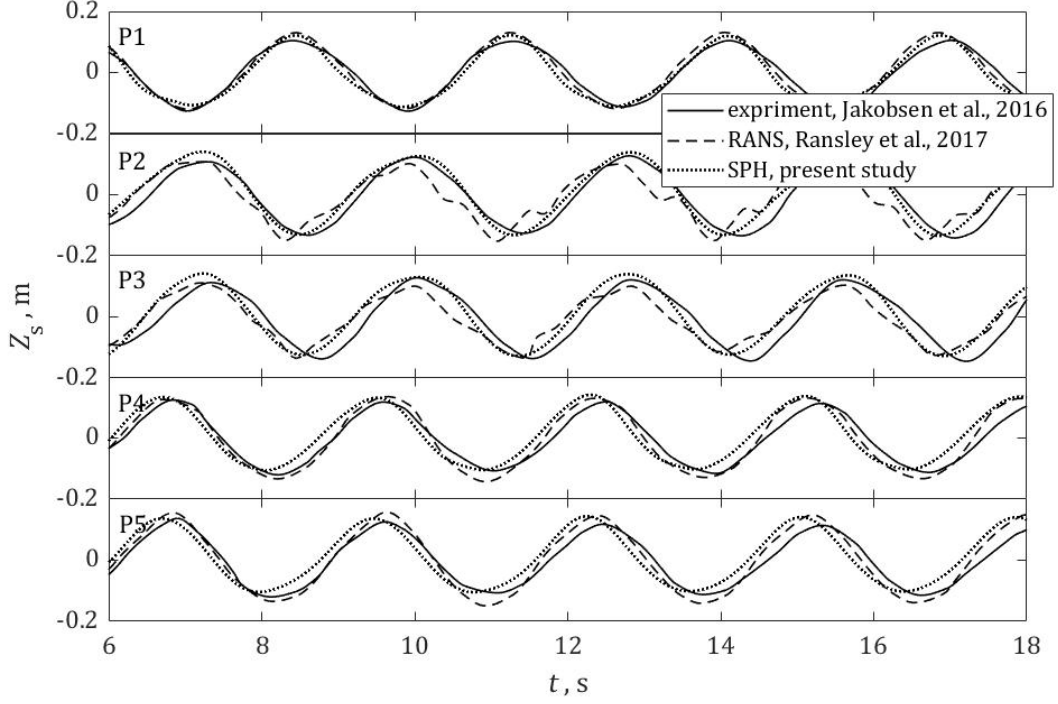


Figure 6: Surface elevation time histories at five probe locations surrounding the fixed device with  $D = 1$  m in regular waves of height  $H = 0.25$  m and period  $T = 2.8$  s.

Fig.6 and fig.7 compare the SPH predictions of surface elevation  $Z_s$  and load components on the device model  $F_x$  and  $F_z$  with the measurements by Jakobsen et al. [24]. In order to allow initial transients to decay, we only consider numerical and experimental results after 6 s (about 2 wave cycles and 33% of total simulation duration) have occurred once wave generation has been initiated.

The results at P1 in fig.6 show that the incident wave is reproduced well, with an amplitude over-estimate of about 2.3% which is smaller than the over-estimate of 10.1% obtained by Ransley et al. [31] using a RANS-VoF model. This suggests that the present SPH method is more accurate than RANS-VoF at reproducing the wave surface behaviour. This also provides confidence in the particle resolution given that there are only 5 acceptable particles over the height of the wave.

The results at P2 and P3 in fig.6 show the surface elevation motions with time in the wake region of the float. It can be seen that the presence of the float does not significantly disturb the free surface downstream. Compared with the RANS

simulation which predicts a high frequency disturbance to the waveform, the SPH simulation gives a smoother representation of the temporal evolution of the surface elevation as would be expected close to the wave maker. The crests simulated by the SPH model are slightly larger than the experimental ones, whereas the troughs are smaller, leading to an amplitude deviation less than 5.4% from the measured results. At the gauge located 2.04 m downstream of the float, the simulated wave has a phase lead of about 20 degrees with respect to the measured wave. However, the amplitude deviation of RANS simulation and the phase lead reach 10.8% and 32 degrees respectively; these accord with the improved prediction by the SPH model.

The results at P4 and P5 in fig.6 show the surface elevation time series to the side of the float. The measured surface elevations along the wave crest almost match the undisturbed incident time series. In the RANS simulation, however, flattening of waveforms and larger wave heights than the incident wave were observed, which were attributed to wave scattering from the float. Compared with the physical water tunnel, the side walls of NWT in the RANS simulation are closer to the float and there is no energy absorption from the waves. Instead, waves scattered from the float are re-reflected between the side walls of the NWT, leading to the observed discrepancies from the measurements. A NWT of the same dimensions is utilised in the SPH simulation; however, wave scattering is not evident through either deformation of the waveform or increase in wave height, though there is a phase lead of 26 degrees.

Fig.7 presents time histories of the horizontal and vertical force components on the float. The experimental observations, present SPH predictions, and previous RANS simulations are superimposed for comparison purposes. In the top panel of fig.7, both SPH and RANS perform well in predicting the asymmetric horizontal force on the fixed device, with the horizontal force increasing more slowly than it decreases. However, the amplitude deviation of the horizontal force obtained by the SPH method is 3.1%, which is smaller than the value of -18.6% obtained by RANS. For the much larger vertical force, the standard deviation of 8.5% peak-peak value between the SPH model predictions and measurements is also smaller than the corresponding standard deviation of 10.3% for the RANS model. This confirms the suitability of the SPH method to predict the temporal evolution of the forces on the device. Besides, the improved performance of SPH is also confirmed by the smaller phase lead incurred between the predicted and experimental waveforms than for the RANS model.

In short, the SPH method provides accurate predictions of the surface elevations in the vicinity of the float and the loads on the float, and reproduces a reliable picture of the relatively complex flows in the case of a fixed device.

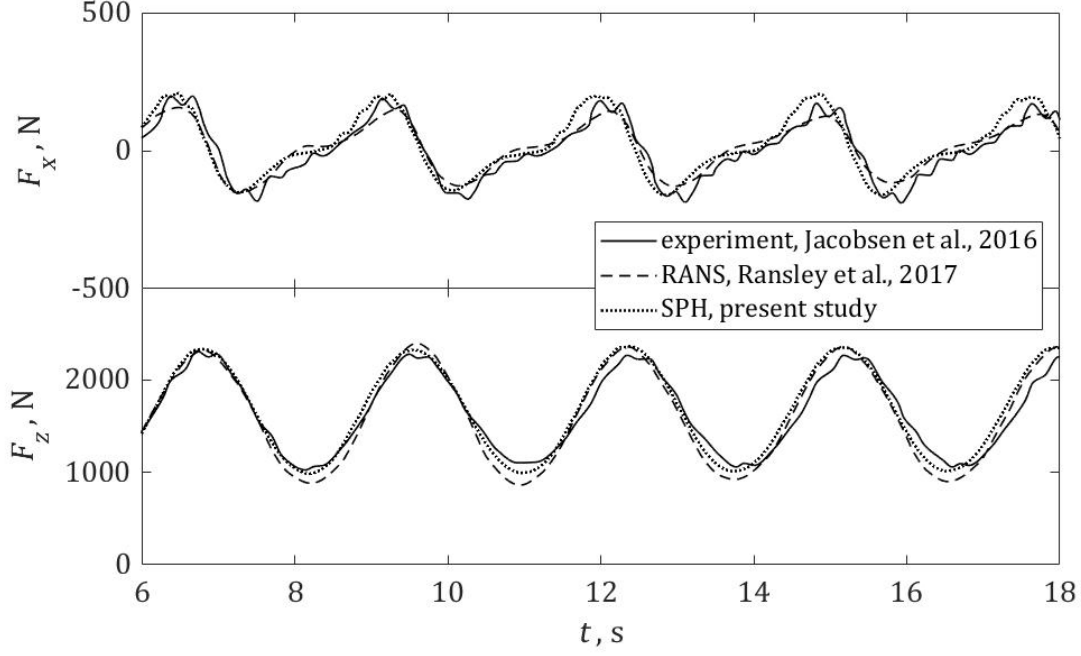


Figure 7: Time histories of horizontal and vertical force components on the float of the fixed device with  $D = 1$  m, in regular waves of height  $H = 0.25$  m and period  $T = 2.8$  s.

### 3.2.2. Freely pitching device

We now simulate the same regular wave case as before, but with the scaled model able to pitch freely about the hinge point between the support structure and the arm, and with the PTO system disabled (i.e. no PTO stiffness and damping). In this case, the motion of the float is coupled to the hydrodynamic loading of the surrounding fluid. The pitching motion is transformed into a single translation of the disabled PTO cylinder within the device constraints, i.e.  $X_c$ . Positive displacement of the cylinder corresponds to lifting of the float. After about 6 s, the different initial transients of the float position in the experiment and simulations by RANS and SPH decay, and the corresponding systems reach a stable oscillatory state driven by the incident wave.

Fig.8 compares the measured and predicted time series of PTO cylinder displacement after 6 s. Compared with measured results, the RANS simulation predicts a larger displacement amplitude, while the SPH simulation predicts less amplitude deviation but with a small phase lead of about 13 degree. Similar to the previous comparison of wave crest elevations for the fixed device, the deviations of SPH and RANS-VoF simulations from measurements on the freely pitching device are due to

443 re-reflection of scattered/radiated waves from the float by side walls of the narrow  
 444 NWT and consequent interference with incident waves at the float location.

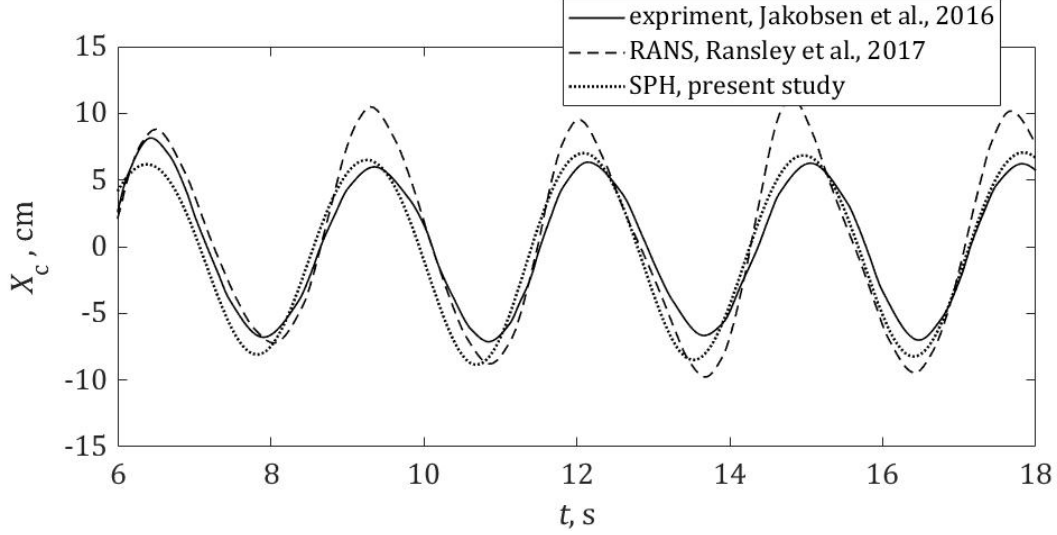


Figure 8: PTO cylinder displacement time history of the freely pitching device with  $D = 1$  m in regular waves of height  $H = 0.25$  m and period  $T = 2.8$  s.

445 Fig.9 compares time series of horizontal and vertical forces obtained from the  
 446 SPH simulation with the available experimental results by Jakobsen et al. [24] from  
 447  $t = 20$  to  $27$  s. This duration is enough to validate the SPH model, because the  
 448 force components have evolved into a steady state and shown the similarity between  
 449 wave cycles. The numerical model provides a satisfactory prediction of the temporal  
 450 evolution of the force components, including their asymmetry. The standard deviation  
 451 between simulated and experimental values of the overall force over 7 s is 7.6%  
 452 peak-peak value of the varied force. The amplitude deviation of the horizontal force  
 453 is -5.7% and the phase lead of the vertical force is approximately zero.

### 454 3.2.3. Extreme waves

455 The foregoing two cases of fixed and freely pitching device by the SPH modelling,  
 456 with  $D = 1$  m, subject to regular waves of height  $H = 0.25$  m and period  $T = 2.8$  s,  
 457 have demonstrated that the SPH model gives an accurate hydrodynamic representa-  
 458 tion of wave height, wave phase, force components, and the device motion. In order  
 459 to test the robustness of the SPH model, a steep regular wave with  $H = 0.68$  m and  
 460  $T = 2.0$  s is simulated with the device still able to move freely. Although Jakobsen  
 461 et al. [24] did not perform tests for freely pitching device in extreme waves to avoid



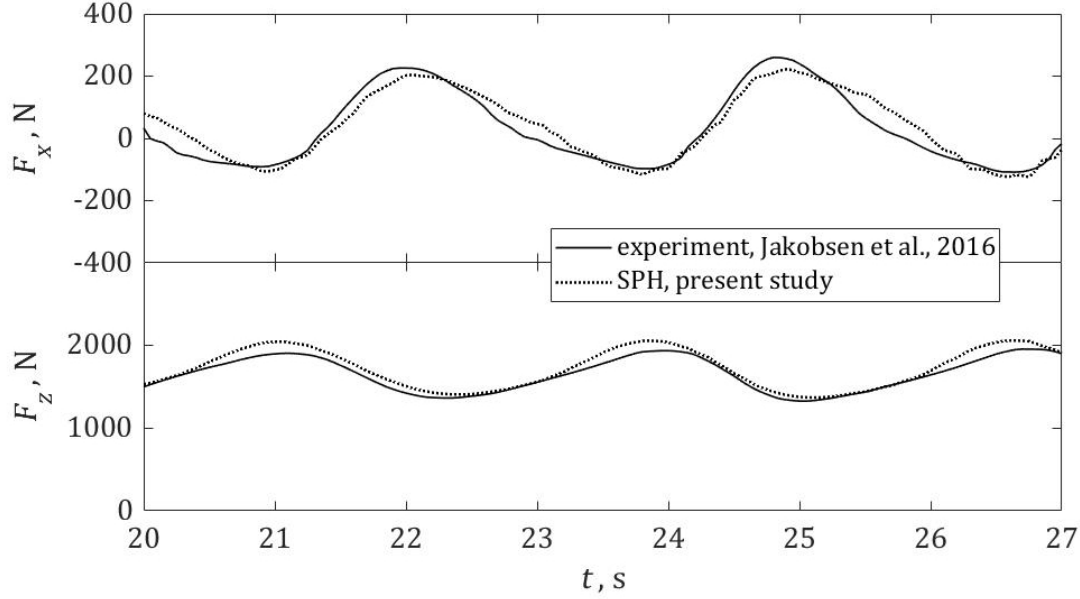


Figure 9: Horizontal (in wave propagation direction) and vertical force components on the float of a freely pitching device with  $D = 1$  m subject to regular waves of height  $H = 0.25$  m and period  $T = 2.8$  s.

possible damage to the device due to excessive motion, Ransley et al. [31] provided RANS-VoF snapshots showing device-wave interaction in this case. We also report a series of SPH snapshots for the three cases with  $D = 1$  m.

Fig.10 and fig.11 respectively illustrate the snapshots of device-wave interaction for the fixed and freely pitching device model in small-steepness waves at 4 instants during a wave cycle. The deformation of free surface neighbouring the float becomes stronger when the wave crest passes by the float, and radiated waves are very weak in these two cases.

Fig.12 illustrates the snapshots for the freely pitching device model in large-steepness waves. During a wave cycle the float goes from being nearly completely submerged to leaving the water altogether. Free surface deformation and radiated waves are stronger in the case of extreme waves than those in the case of small-steepness waves. The phenomenon of green water is observed when the float is pitching from the trough elevation to the peak elevation, and the phenomenon of slamming is observed when the float is pitching from the peak elevation to the trough elevation. In addition, spray is observed upstream the float at the peak elevation. These complex phenomena are handled by the present SPH simulation without issue,

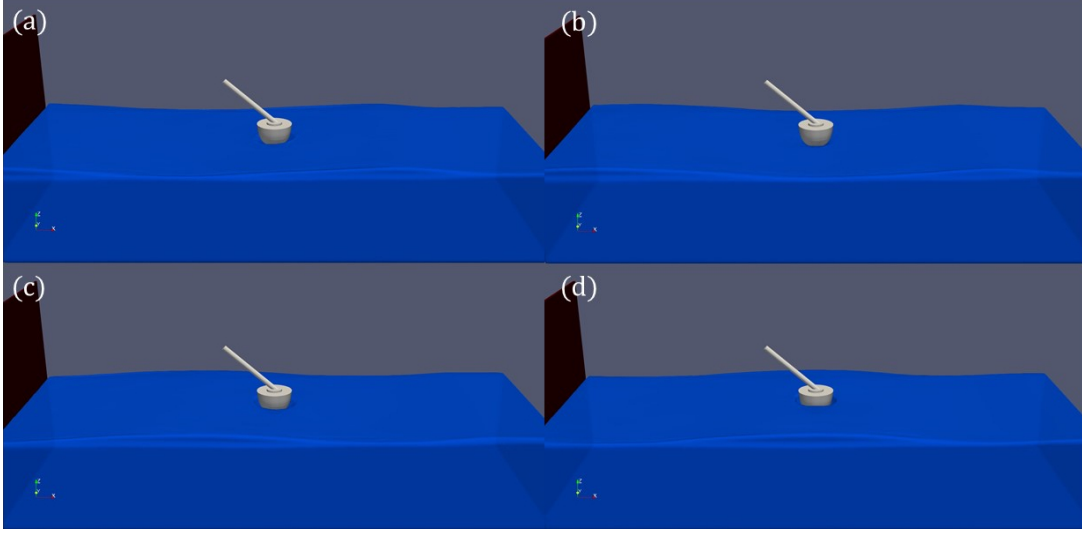


Figure 10: Snapshots of the fixed device with  $D = 1$  m subject to small-steepness waves of height  $H = 0.25$  m and period  $T = 2.8$  s. (a) and (c) the mid wave elevations close to the float, (b) and (d) the maximum and minimum wave elevations.

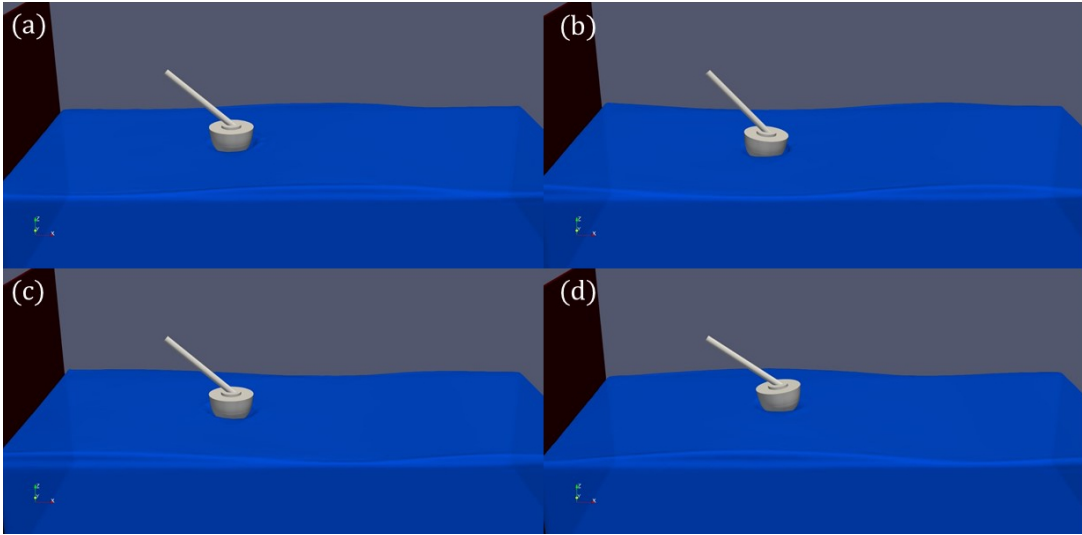


Figure 11: Snapshots of the freely pitching device with  $D = 1$  m subject to small-steepness waves of height  $H = 0.25$  m and period  $T = 2.8$  s. (a) and (c) the mid float elevations, (b) and (d) the maximum and minimum float elevations.

479 meaning the robustness of the SPH model. The resulting observations are consistent  
 480 with the numerical results by Ransley et al. [31], which further provides confidence

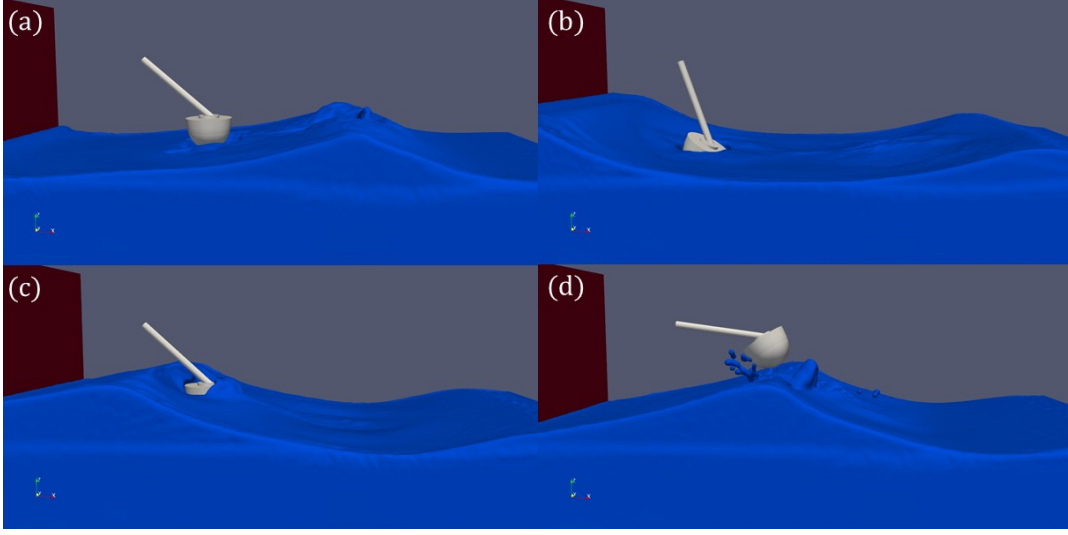


Figure 12: Snapshots of the freely pitching device with  $D = 1$  m subject to large-steepness waves of height  $H = 0.68$  m and period  $T = 2.0$  s. (a) and (c) the mid float elevations, (b) and (d) the maximum and minimum float elevations.

481 in predicting the power conversion performance of a top-mounted pitching point  
 482 absorber.

#### 483 4. Predicted power conversion performance of devices at different scales

484 A parameter study is next undertaken for the power conversion performance  
 485 of the top mounted pitching point absorber with the PTO system engaged. The  
 486 NWT and device are simulated at different scales using a similar numerical setup as  
 487 above (see fig.5 and table 2). We assume that the configuration of the small-scale  
 488 NWT and device in Section 3.1 is valid across different scales and with the PTO  
 489 engaged [67, 68]. The influence of wave conditions (wave height and period) on  
 490 power conversion performance and on the PTO damping coefficient are considered.

491 The PTO is modelled as a spring-damping system that links the support structure  
 492 and the arm of the pitching device as shown in fig.2, with zero stiffness and adjustable  
 493 damping, governed by Newton's second law:

$$M \frac{d\vec{v}_r}{dt} = \vec{F}_e + \vec{F}_d, \quad (6)$$

494 where  $M$  and  $\vec{v}_r$  are the mass and relative velocity of the PTO,  $\vec{F}_d$  is the damping  
 495 force, and  $\vec{F}_e$  is the excitation force exerted by the pitching point absorber. The

496 linear damping is adopted, i.e. the damping force is written as

$$\vec{F}_d = -C\vec{v}_r, \quad (7)$$

497 where  $C$  is the damping coefficient. Note that  $C$  approaches infinity for a fixed  
 498 pitching device, whereas  $C$  is zero for a freely pitching device. PTO damping is the  
 499 mechanical force that extracts power from the wave-induced motion of a pitching  
 500 float. In order to improve the energy conversion efficiency, the PTO system is de-  
 501 signed to run in slow relative motion with limited mass such that the inertial force is  
 502 negligible compared to the damping force. Accordingly, the power absorbed by the  
 503 device can be estimated by the PTO damping as follows:

$$P = \frac{1}{3T} \sum_{n=1}^{3T/\Delta t} C\vec{v}_{rn} \cdot \vec{v}_{rn} \Delta t = \frac{1}{3T} \sum_{n=1}^{3T/\Delta t} C|\vec{v}_{rn}|^2 \Delta t, \quad (8)$$

504 where  $P$  is the absorbed power,  $T$  is the wave period,  $\Delta t$  is the time step specified  
 505 as 0.05 s, and  $\vec{v}_{rn}$  is the relative velocity vector at time step  $n$ . The total summing  
 506 time is specified as the last three steady wave periods. Note that energy losses in  
 507 the power conversion system and in the transmission system are neglected, i.e. 100%  
 508 PTO efficiency is adopted. In addition to the converted power  $P$ , the quantity CWR  
 509 [16] is introduced here to quantify the performance of the device according to its  
 510 scale dimension and the incident wave conditions:

$$\text{CWR} = \frac{P}{DP_w}, \quad (9)$$

511 where  $D$  is the referential diameter of the device and  $P_w = \rho g^2 H^2 T / 32\pi$  is the  
 512 incident power in regular waves of wave height  $H$  and period  $T$ .  $\rho$  is water density,  
 513 and  $g$  is the acceleration due to gravity.

#### 514 4.1. Device with $D = 1$ m

515 This section examines wave energy conversion by a device with  $D = 1$  m in  
 516 regular incident waves. Fig.13 shows the time series of the magnitude of the relative  
 517 velocity vector  $|\vec{v}_r|$  in the top panel and the PTO absorbed power  $P$  in the bottom  
 518 panel for varying damping coefficients in the range of  $0 \leq C \leq 8 \times 10^4$  Ns/m with  
 519  $H = 0.25$  m and  $T = 2.8$  s. The amplitude of  $|\vec{v}_r(t)|$  is observed to decrease with  
 520 increasing  $C$ . Compared to the kinematics of the freely pitching device, a time delay  
 521 occurs for the damped device with the PTO enabled, and the time delay is observed  
 522 to increase along with  $C$ . Different from the above-mentioned monotonous changes  
 523 caused by the PTO damping,  $P$  first increases rapidly and then gradually decreases

with increasing  $C$ . The peak power over the damping coefficient range is located at  $C = 2.0 \times 10^4$  Ns/m, exhibiting a uni-modal distribution of  $P$  in terms of  $C$ . This uni-modal distribution means the short-term optimal operation of the device with a certain wave period can be achieved by adjusting the PTO damping. Accordingly, three damping coefficients respectively smaller than, equal to and larger than the damping coefficient absorbing the most power are studied for each scaled device to give insights into the effects of  $T$  and  $H$  on the wave conversion performance.

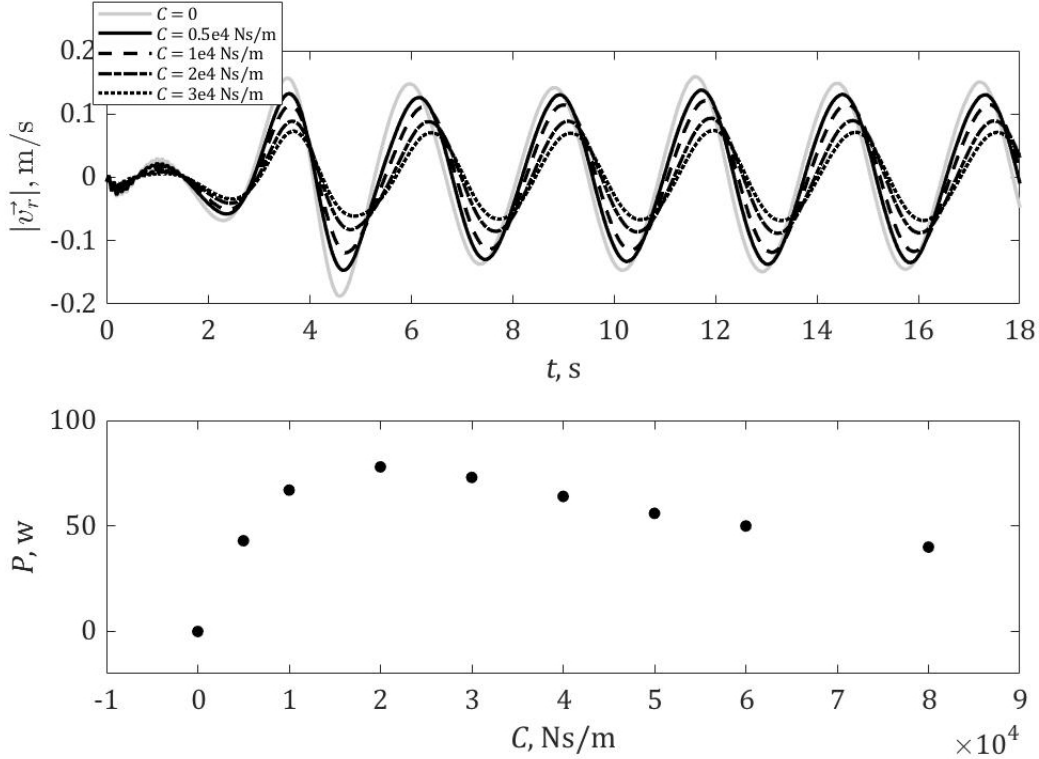


Figure 13: Top: time series of  $|\vec{v}(t)|$  for  $C = 0, 0.5, 1.0, 2.0$ , and  $3.0 \times 10^4$  Ns/m (gray solid, black solid, dashed, dash-dotted, dotted lines); bottom:  $P$  versus  $C$ .  $D = 1$  m,  $H = 0.25$  m and  $T = 2.8$  s.

Fig.14 presents the standard deviation value of damping force  $\sigma(F_d)$ , the PTO absorbed power  $P$ , and the capture width ratio CWR with varying wave period  $T$  for wave heights  $H = 0.25$  and  $2.0$  m and damping coefficients  $C = 1.0, 2.0$ , and  $6.0 \times 10^4$  Ns/m. In all cases reported in fig.14,  $\sigma(F_d)$  and  $P$  have the same trend, i.e. they increase first and then decrease with increasing  $T$ . The reason for the same trend is that in the case of ideal PTO, damping forces balance PTO excitation forces exerted by the float and directly do work to produce the output power with the

intrinsic relation of  $\sigma(F_d) = \sqrt{CP}$ . Only one peak occurs over the period range of simulated waves, exhibiting a uni-modal distribution of  $\sigma(F_d)$  and  $P$  in terms of  $T$ . The wave periods at which the peaks of  $\sigma(F_d)$  and  $P$  occur are the same, and are found to increase with PTO damping.

The uni-modal behaviours of  $P$  with  $C$  and  $T$  implies that a one-to-one correspondence of  $C$  and  $T$  exists for the peak  $P$ . This is meaningful for the targeted operation of the PTO system to achieve the short-term optimal energy conversion performance with varying wave period. Specifically, the PTO damping coefficient should be adjusted to a corresponding larger value for an increased wave period, and to a certain smaller value for a decreased wave period. A PTO with a damping coefficient of  $C = 2.0 \times 10^4$  Ns/m absorbs more energy from waves of period in the range of  $1 < T < 5$  s than PTOs with other damping coefficients, which is proved to be the global optimal PTO damping for the device with  $D = 1$  m. Furthermore, the peak absorbed power with the optimal damping is found to be the largest one among those power peaks with different damping coefficients. For  $C = 2.0 \times 10^4$  Ns/m, the power peak occurs at wave period  $T = 2.8$  s. This optimal wave period (2.8 s) is noted to be larger than the natural period (1.9 s) of the freely pitching device.

Although more power is captured from waves of  $H = 2.0$  m by a PTO with fixed  $C$ , the normalised quantity CWR is larger for  $H = 0.25$  m. In addition, the wave period corresponding to the CWR peak is no larger than that corresponding to the power peak for different  $H$  and  $C$ . The different behaviours of  $P$  and CWR with  $H$  and  $T$  can be explained by dimensional analysis. According to the definition of CWR, the effect of  $H$  and  $T$  on CWR is written as  $CWR(H, T) \sim P(H, T)/TH^2$ . For the same  $T$  and  $C$ , the ratio of  $P$  with  $H = 2.0$  m over  $P$  with  $H = 0.25$  m is basically a constant of 24.0, leading to a constant shift between  $P$  curves with different  $H$  and the same  $C$  in the middle panel of fig.14. Hence, the ratio of CWR with  $H = 2.0$  m over CWR with  $H = 0.25$  m is 0.375 for fixed  $T$  and  $C$ . Also because  $CWR(T) \sim P(T)/T$ , the peak CWR moves at smaller  $T$  compared to the peak  $P$  for fixed  $C$  and  $H$ .

As wave steepness progressively increases with larger wave height for a fixed wave period, or with smaller wave period for a fixed wave height, nonlinear interaction between the device and waves increasingly strengthens under the influence of slamming and green water processes. For the device with enabled PTO, the PTO damping also affects the occurrence of these complex phenomena. Compared with the freely pitching device, the pitching movement of the float is damped when the PTO system is absorbing the wave energy. Hence, the green water become stronger while the slamming become weaker with increased PTO damping. Despite the hydrodynamic complexity at large wave steepness and varying PTO damping, the SPH

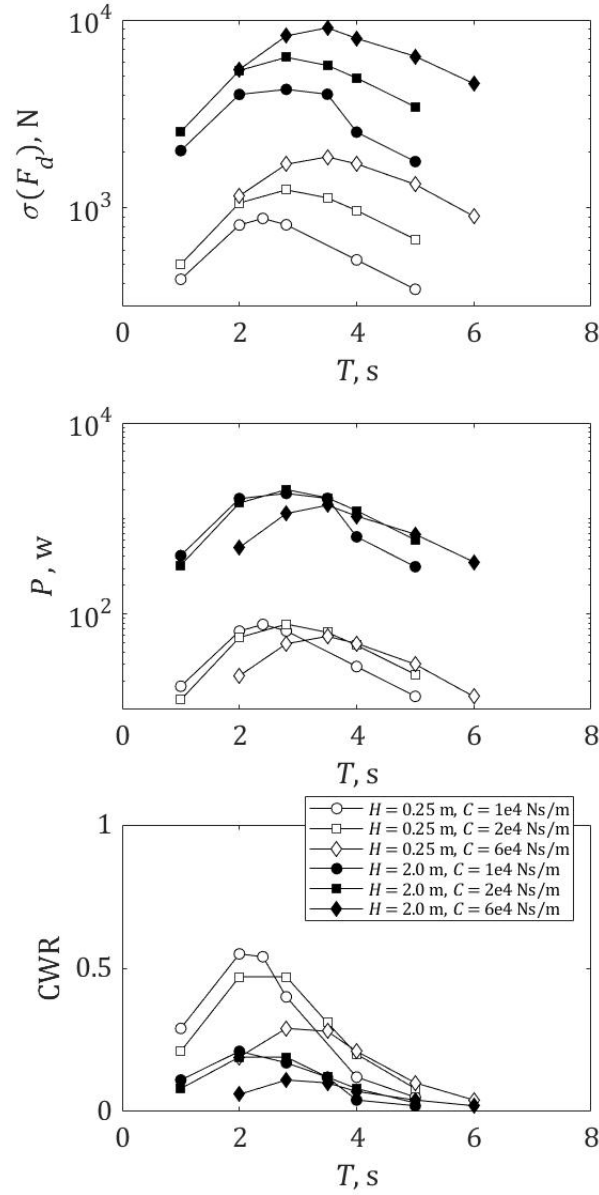


Figure 14: Wave energy conversion performance (upper plot:  $\sigma(F_d)$ ; middle plot:  $P$ ; lower plot: CWR) as a function of  $T$  for  $H = 0.25$  and  $2.0$  m (open, closed symbols) and  $C = 1.0, 2.0$ , and  $6.0 \times 10^4$  Ns/m (circle, square and diamond symbols).  $D = 1$  m.

576 model nevertheless remains reliable and stable.

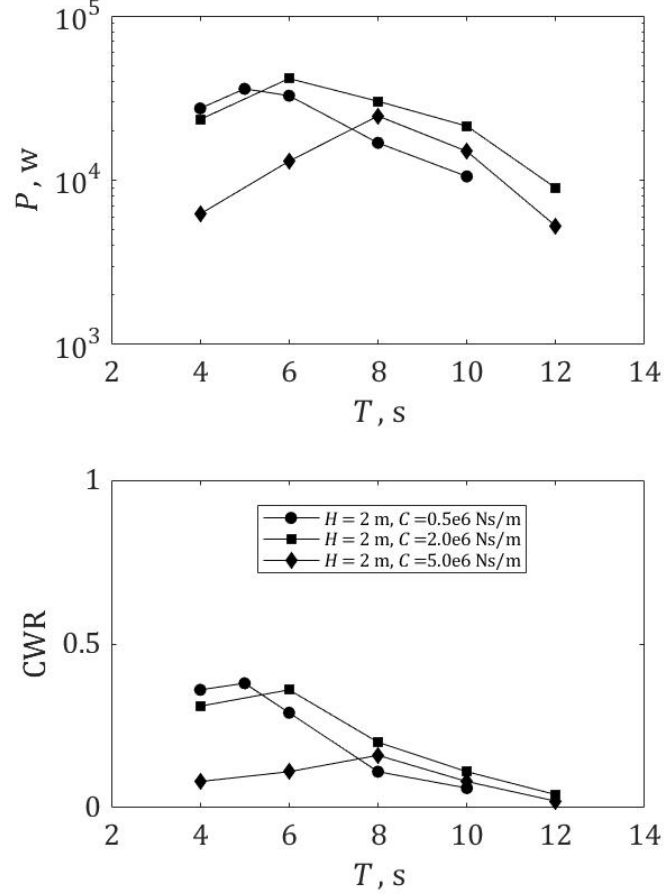


Figure 15: Wave energy conversion performance (upper plot:  $P$ ; lower plot: CWR) as a function of  $T$  for  $H = 2.0$  m and  $C = 0.5, 2.0$ , and  $5.0 \times 10^6$  Ns/m (circle, square and diamond symbols).  $D = 5$  m.

578 We next consider a device with  $D = 5$  m subject to waves with the constant height  
 579 of  $H = 2$  m. The natural period of the device is 4.2 s. At the initial moment, the  
 580 water-plane diameter of this scaled device is 4.9 m and the draught is 2.0 m. Fig.15  
 581 displays the influence of PTO damping coefficient on the wave energy conversion  
 582 performance curves. The reported damping coefficients  $C = 0.5, 2.0$ , and  $5.0 \times$   
 583  $10^6$  Ns/m are chosen according to the same criterion as in the case of  $D = 1$  m,  
 584 and the uni-modal distribution of absorbed power with wave period is observed



for different damping coefficients. The power converted by a single point absorber with  $D = 5$  m reaches a maximum of 42 kW when the PTO damping coefficient is  $2.0 \times 10^6$  Ns/m. Although the damping coefficient of  $C = 0.5 \times 10^6$  Ns/m is better for  $4 \leq T \leq 5$  s,  $C = 2.0 \times 10^6$  Ns/m gives the best performance in the wider wave period range of  $4 \leq T \leq 12$  s. The same trend of  $P$  with  $T$  applies to the CWR curves. It is noted that the CWR peak with the optimal damping is not the maximum among those with different  $C$  for  $D = 5$  m. The inconsistent behaviours of  $P$  and CWR are attributed to the coupled effects of  $T$  and  $C$  according to the relation of  $\text{CWR}(T, C) \sim P(T, C)/T$  as drawn for  $D = 1$  m.

#### 4.3. Device with $D = 1 \sim 10$ m

To examine scale effect on energy conversion performance, simulations are carried out for devices with  $D$  ranging from 1 to 10 m in regular incident waves of height  $H = 2$  m. For the device with  $D = 10$  m, the natural period is 6.0 s and the initial draught and water-plane diameter are respectively 4.0 m and 9.8 m. We also observe the uni-modal distribution of absorbed power versus wave period for  $D = 10$  m as in the cases of  $D = 1, 5$  m. By searching for the highest one among the peaks of the uni-modal distributions with different  $C$ , we achieve the optimal damping for each scaled device. All these devices operate under optimal damping of absorbed power; in other words  $C_o = 2 \times 10^4$  Ns/m for  $D = 1$  m,  $C_o = 2 \times 10^6$  Ns/m for  $D = 5$  m and  $C_o = 5 \times 10^7$  Ns/m for  $D = 10$  m, where the subscript  $o$  indicates optimal. The upper panel of fig.16 shows the uni-modal distribution of  $P$  with  $T$  for  $D = 1 \sim 10$  m. Both the absorbed power and the wave period pertaining to the peak of the uni-modal distribution increase with the increasing device scale. The results indicate that a device with  $D = 10$  m generates about 10 times more power than a device with  $D = 5$  m and 300 times more than a device with  $D = 1$  m. As  $D$  increases from 1 to 10 m, CWR increases from 0.2 to about 1.0, implying that the larger device, when optimally damped, can absorb energy from longer incident waves with fixed wave height.

## 5. Discussion of optimal power

### 5.1. Scale effect

An understanding of scale effect on optimal absorbed power is important in device design. Here, optimal power  $P_o$  and associated wave period  $T_o$  are identified from the power curves of devices with different float diameters  $D$  and corresponding optimal damping coefficients  $C_o$  (see fig.16). The upper plot in fig.17 shows the behaviour of  $P_o$ ,  $T_o$  and  $C_o$  with varying  $D$ . Linear fits have been made to the simulated results in

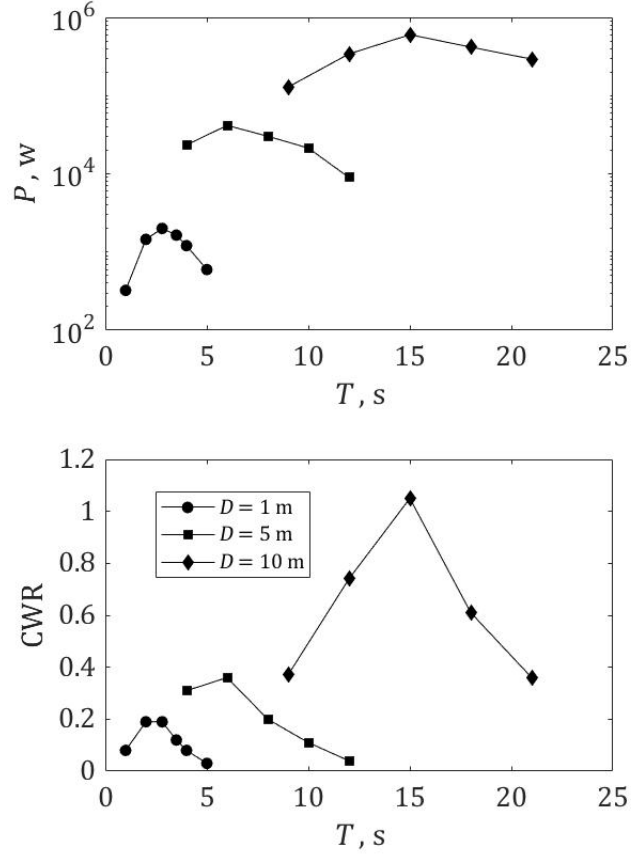


Figure 16: Wave energy conversion performance (upper plot:  $P$ ; lower plot: CWR) as a function of wave period  $T$  under optimised PTO damping conditions for  $D = 1, 5$ , and  $10$  m indicated by circle, square and diamond symbols.

the log-log plot, and the following empirical relationships obtained from the limited data:

$$\begin{aligned}
 P_o &\propto 1.58 \times 10^3 \cdot D^{2.4}, \\
 T_o &\propto 2.51 \cdot D^{0.7}, \\
 C_o &\propto 1.58 \times 10^4 \cdot D^{3.3}.
 \end{aligned} \tag{10}$$

The above empirical relations are limited to regular incident wave conditions of constant height and period, and to a PTO system with zero-stiffness, linear damping, and 100% efficiency. These are obvious simplifications compared to actual field deployment situations. Even so, the scaling relations inherently include hydrodynamic

626 Froude number  $Fr$  and Reynolds number  $Re$  effects and the dynamic effect of the  
 627 PTO itself. For the freely pitching device, the  $Fr$  scaling law is dominant and the  
 628  $Re$  scaling law is of very minor importance under typical operating wave conditions.  
 629 However, for the device with enabled PTO, the hydrodynamics of the float and the  
 630 dynamics of the PTO are coupled together to form a more complicated system. In  
 631 addition to  $Fr&Re$  effects, the effect of PTO damping should be considered.

632 Through dimensional analysis, the absorbed power, the wave period, and the  
 633 PTO damping are respectively proportional to  $D^{3.5}$ ,  $D^{0.5}$  and  $D^2$  solely according  
 634 to the  $Fr$  scaling law, while are proportional to  $D^2$ ,  $D^2$  and  $D^5$  solely according  
 635 to the  $Re$  scaling law. The observed scaling behaviours of the optimal absorbed  
 636 power ( $P_o \sim D^{2.4}$ ), wave period ( $T_o \sim D^{0.7}$ ), and damping coefficient ( $T_o \sim D^{3.3}$ )  
 637 deviate from the  $Fr$  scaling law which dominates the hydrodynamics of the freely  
 638 pitching device. These deviations should be due to the coupled effect of the PTO  
 639 damping. However, neither well-defined dimensionless quantity (e.g. damping ratio  
 640 in a spring-damping-oscillator system) nor corresponding scaling law (similar to the  
 641 hydrodynamic  $Fr&Re$  laws) is available to characterise the damping effect in the  
 642 PTO system with zero-stiffness. Hence, further quantitative studies on the device  
 643 performance with enabled PTO are needed to resolve the combined scaling effects.

## 644 5.2. Effect of water depth

645 Among physical conditions at the deployment site of a WEC, the water depth  
 646 is a basic one relevant for wave energy conversion. The effect of water depth  $h$  on  
 647 energy conversion with optimal PTO damping is now discussed briefly. According  
 648 to the linear potential theory for unconstrained axisymmetrical point absorbers [69],  
 649 the upper limit of absorbed power by an optimally controlled float is  $P_w \lambda_I / 2\pi$ , where  
 650  $\lambda_I$  is the regular wave length as  $h \rightarrow \infty$ . This power limit is independent of float  
 651 diameter. Then, the theoretical CWR at the upper power limit is

$$\text{CWR}_{th} = \frac{P_w \lambda_I / 2\pi}{P_w D} = \frac{gT^2}{4\pi^2 D}. \quad (11)$$

652 Note that  $\text{CWR}_{th}$  is essentially the limit efficiency of a point absorber deployed in  
 653 the deep water.

654 The lower plot of fig.17 shows the relationship between  $\text{CWR}/\text{CWR}_{th}$  and  $h \times$   
 655  $2\pi/\lambda$  (where  $\lambda$  is the wavelength in water of finite depth  $h$ ), which indicates the in-  
 656 fluence of dimensionless water depth on energy conversion efficiency with the optimal  
 657 PTO damping. For  $D = 1, 5$  m,  $\text{CWR}/\text{CWR}_{th}$  monotonically increases along with  
 658  $2\pi h/\lambda$  in the range of  $0.7 < 2\pi h/\lambda < 12$ . Waves travelling from deep water to shal-  
 659 low water suffer increasingly from bottom friction, making less available wave energy.

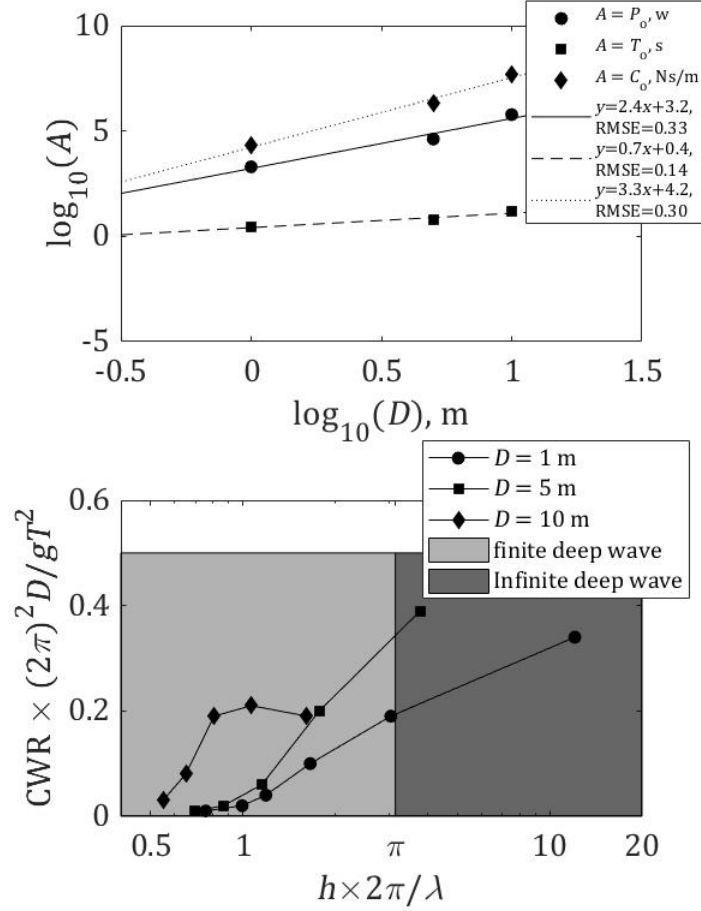


Figure 17: Upper plot: log-log optimal  $P_o$  (circle),  $T_o$  (square) and  $C_o$  (diamond) as functions of  $D$ . Corresponding linear fits are presented as solid, dashed, and dotted lines. Lower plot:  $CWR/CWR_{th}$  as a function of  $h \times 2\pi/\lambda$  for  $D = 1, 5, 10$  m (circle, square and diamond symbols) in water depth that is infinite (dark) and finite (light).

Assumed that a device with a fixed PTO damping has a fixed energy conversion ability, the wave energy conversion efficiency  $CWR$  gradually increases to its limit value  $CWR_{th}$  with increasing water depth. However, for  $D = 10$  m, a local optimal water depth seems to exist close to  $2\pi h/\lambda = 1.1$ . This trend with dimensionless water depth in the finite deep water is consistent with the linear inviscid modelling of a heaving buoy by Garnaud & Mei [70, 71], but the viscous effect leads to relatively low efficiency in the present SPH modelling. It is worthy of further study whether an in-

creasing trend of  $CWR/CWR_{th}$  with  $2\pi h/\lambda$  can be achieved in the infinite deep water for the larger device. In addition, it is noted that the larger device always converts wave energy with higher efficiency in the range of  $0.5 < 2\pi h/\lambda < 1.6$  compared with the smaller ones. In deep water ( $2\pi h/\lambda > \pi$ ), waves travel almost without energy loss across the ocean, and predictions of device performance by testing and modelling are easy to transfer for siting. However, devices in shallow water ( $2\pi h/\lambda < \pi/10$ ) have different structural solutions and facilitated access to grid connection and equipment maintenance with low costs. Taking into consideration a trade-off of available energy and costs, the most appropriate site for a top-mounted pitching point absorber is usually in finite deep water ( $\pi/10 < 2\pi h/\lambda < \pi$ ). Hence, the peak efficiency of the larger device at water depth of  $2\pi h/\lambda = 1.1$  provides reference for device siting.

## 6. Conclusions

Owing to its inherent advantages in capturing rapidly deforming free surface flows, a meshless SPH model was used to investigate the power conversion performance of a top-mounted pitching point absorber. The SPH model gave free surface motions in satisfactory agreement with experimental measurements of wedge entry into otherwise still water, properly representing extreme free surface motion events during the wedge immersion stages, including slamming, green water, splash, break-up, and recombination. For a geometrically complex wave energy conversion device such as Wavestar, accurate modelling of the interaction between water free surface and device is key to solving the overall fluid-structure problem, which is important in survivability and performance assessments.

The SPH simulations show good agreement with the measurements and the RANS-VoF predictions of characteristic hydrodynamic behaviours of fixed and freely pitching devices fitted with an 1 m diameter absorber subject to the same incident wave conditions. Only limited phase leads were found in the SPH simulations of the surface elevation beside the fixed model and the PTO displacement of the freely pitching model. In the case of extreme waves, the SPH modelling demonstrates the robustness and handles the complex phenomena such as green water, spray and slamming without issue. Execution times of the SPH simulations were not increased significantly despite the wave-float-coupled kinematics and the large wave steepness. The satisfactory prediction accuracy and limited computational costs of the SPH simulations provide confidence in further studying the power conversion performance of the top-mounted pitching point absorber.

A study of wave energy conversion performance under different wave conditions and PTO damping coefficients revealed that: absorbed power  $P$  invariably had a

uni-modal distribution with damping coefficient  $C$  and wave period  $T$  over the range of test cases considered; the wave period corresponding to peak absorbed power increased with the PTO damping. The uni-modal behaviours of  $P$  with  $C$  and  $T$  is meaningful for the targeted operation of the PTO system to achieve the short-term optimal energy conversion performance with varying wave period. In addition, inconsistent behaviours of absorbed power  $P$  and capture width ratio CWR with varied wave height  $H$  were observed, which can be explained according to the relation  $CWR(H, T, C) \sim P(H, T, C)/TH^2$ .

A further study examined the effects of scale and water depth on energy conversion with optimal PTO damping. It was found that a device with  $D = 10$  m generated about 300 times more power than one with  $D = 1$  m. As  $D$  increased from 1 m to 10 m, CWR increased from 0.2 to about 1.0, implying that a larger device that is optimally damped is increasingly effective at absorbing energy from long incident waves of maximum wave height. Optimal absorbed power, wave period and PTO damping exhibited a power law relationship with device scale. Because of the combined  $Fr$  &  $Re$  effects and the PTO damping effect, scaling behaviours of the optimally damped pitching device deviate from the  $Fr$  scaling law which dominates the hydrodynamics of the freely pitching device. In terms of water depth, a small device ( $D = 1, 5$  m) appears higher efficiency of extracting energy from deep water waves than from shallower water waves, whereas a large device ( $D = 10$  m) achieves the maximum efficiency in water of finite depth provided  $0.5 < 2\pi h/\lambda < 1.6$ . In the water of finite depth, the larger device always converts wave energy with higher efficiency compared with the smaller ones. The peak efficiency of the larger device at water depth of  $2\pi h/\lambda = 1.1$  provides reference for device siting.

## Acknowledgements

This work was supported by the National Key Research and Development Plan of China (Nos. 2019YFB1504402, 2017YFE0132000 and 2018YFB1501202), the National Natural Science Foundation of China (No. 11872248) and the Self-directed Research Subject of the State Key Laboratory of Marine Engineering, Shanghai Jiao Tong University (No. GKZD010075). The authors would like to thank Hongliang Wang and Jianguo Gong for their assistance in the experiments.

## References

- [1] C. V. C. Weiss, R. Guanche, B. Ondiviela, O. F. Castellanos, J. Juanes, Marine renewable energy potential a global perspective for offshore wind and wave exploitation, *Energy Convers. Manage.* 177 (2018) 43–54.

- [2] A. F. d. O. Falcão, Wave energy utilization: a review of the technologies, *Renew. Sustain. Energy Rev.* 14 (2010) 899–918.
- [3] Wave Dragon, Prototype testing in Denmark, <http://www.wavedragon.net/prototype-testing-in-denmark> (2009).
- [4] S. Oliveira-Pinto, F. Taveira-Pinto, T. Morais, P. Rosa-Santos, Experimental evaluation of the effect of wave focusing walls on the performance of the sea-wave slot-cone generator, *Energy Convers. Manage.* 110 (2016) 165–175.
- [5] A. Al-Habaibeh, D. Su, J. McCague, A. Knight, An innovative approach for energy generation from waves, *Energy Convers. Manage.* 51 (2010) 1664–1668.
- [6] Ocean Power Technologies, PB3 POWERBUOY, <https://oceanpowertechnologies.com/pb3-powerbuoy> (2011).
- [7] R. Curran, T. J. T. Whittaker, T. P. Stewart, Aerodynamic conversion of ocean power from wave to wire, *Energy Convers. Manage.* 39 (1998) 1919–1929.
- [8] Tethys, OES-Environmental Metadata - Oceanlinx MK3, <https://tethys.pnnl.gov/project-sites/oceanlinx-mk3> (2016).
- [9] Energy Island, Lilypad - Wave Energy Conversion, <http://www.energyisland.com/projects/lilypad/lilypad.html> (2009).
- [10] Y. Li, Y. H. Yu, A synthesis of numerical methods for modeling wave energy converter-point absorbers, *Renew. Sust. Energ. Rev.* 16 (2012) 4352–4364.
- [11] Y. Liu, Y. Li, F. He, H. Wang, Comparison study of tidal stream and wave energy technology development between China and some Western Countries, *Renew. Sustain. Energy Rev.* 76 (2017) 701–716.
- [12] World Energy Council, World Energy Perspective, Cost of Energy Technologies, [https://www.worldenergy.org/assets/downloads/WEC\\_J1143\\_CostofTECHNOLOGIES\\_021013\\_WEB\\_Final.pdf](https://www.worldenergy.org/assets/downloads/WEC_J1143_CostofTECHNOLOGIES_021013_WEB_Final.pdf) (2013).
- [13] Y. Li, B. J. Lence, S. M. Calisal, An integrated model for estimating energy cost of a tidal current turbine farm, *Energy Convers. Manage.* 52 (2011) 1677–1687.
- [14] Y. Li, L. Willman, Feasibility analysis of offshore renewables penetrating local energy systems in remote oceanic areas - A case study of emissions from an electricity system with tidal power in Southern Alaska, *Applied Energy* 117 (2014) 42–53.

- 769 [15] R. Carballo, G. Iglesias, A methodology to determine the power performance of  
770 wave energy converters at a particular coastal location, *Energy Convers. Man-*  
771 *age*. 61 (2012) 8–18.
- 772 [16] A. Babarit, A database of capture width ratio of wave energy converters, *Renew.*  
773 *Energy* 80 (2015) 610–628.
- 774 [17] A. Babarit, J. Hals, M. M. J., A. Kurniawan, T. Moan, J. Krokstad, Numerical  
775 benchmarking study of a selection of wave energy converters, *Renew. Energy* 41  
776 (2012) 44–63.
- 777 [18] M. M. Jakobsen, G. Iglesias, M. M. Kramer, V. E., Experimental study of  
778 forces on point absorber, in: 5th International Conference on The Application  
779 of Physical Modelling to Port and Coastal Protection, 2014, pp. 15–24.
- 780 [19] C. Perez-Collazo, D. Greaves, G. Iglesias, Hydrodynamic response of the WEC  
781 sub-system of a novel hybrid wind-wave energy converter, *Energy Convers. Man-*  
782 *age*. 171 (2018) 307–325.
- 783 [20] S. Oliveira-Pinto, P. Rosa-Santos, F. Taveira-Pinto, Assessment of the potential  
784 of combining wave and solar energy resources to power supply worldwide offshore  
785 oil and gas platforms, *Energy Convers. Manage.* 223 (2020) 113299.
- 786 [21] B. Jiang, X. Li, S. Chen, Q. Xiong, B. Chen, R. G. Parker, L. Zuo, Performance  
787 analysis and tank test validation of a hybrid ocean wave-current energy converter  
788 with a single power takeoff, *Energy Convers. Manage.* 224 (2020) 113268.
- 789 [22] L. Berggren, M. Johansson, Hydrodynamic coefficients of a wave energy device  
790 consisting of a buoy and a submerged plate, *Appl. Ocean Res.* 14 (1992) 51–58.
- 791 [23] M. Kramer, L. Marquis, P. Frigaard, Performance evaluation of the Wavestar  
792 prototype, in: 9th European Wave and Tidal Energy Conference, 2011, pp. 5–9.
- 793 [24] M. M. Jakobsen, S. Beatty, G. Iglesias, M. M. Kramer, Characterization of loads  
794 on a hemispherical point absorber wave energy converter, *Int. J. Mar. Energy*  
795 13 (2016) 1–15.
- 796 [25] M. Penalba, A. Mérigaud, J.-C. Gilloteaux, J. V. Ringwood, Influence of non-  
797 linear Froude-Krylov forces on the performance of two wave energy points ab-  
798 sorbers, *J. Ocean Eng. Mar. Energy* 3 (2017) 209–220.



- [26] S. Jin, R. J. Patton, B. Guo, Viscosity effect on a point absorber wave energy converter hydrodynamics validated by simulation and experiment, *Renew. Energy* 129 (2018) 500–512.
- [27] Y. Yu, Y. Li, Preliminary results of a RANS simulation for a floating point absorber wave energy system under extreme wave conditions, in: *Proceedings of the ASME 30th International Conference on Ocean, Offshore, and Arctic Engineering*, 2011, pp. 1–8.
- [28] Q. Xu, Y. Li, Y. Yu, B. Ding, Z. Jiang, Z. Lin, B. Cazzolato, Experimental and numerical investigations of a two-body floating-point absorber wave energy converter in regular waves, *J. Fluid Struct.* 91 (2019) 102613.
- [29] O. M. Faltinsen, M. Greco, M. Landrini, Green water loading on a FPSO, *J. Offshore Mech. Arct. Eng.* 124 (2002) 97–103.
- [30] Y.-H. Yu, Y. Li, Reynolds-Averaged Navier–Stokes simulation of the heave performance of a two-body floating-point absorber wave energy system, *Comput. Fluids* 73 (2013) 104–114.
- [31] E. J. Ransley, D. M. Greaves, A. Raby, D. Simmonds, M. M. Jakobsen, M. Kramer, RANS-VOF modelling of the Wavestar point absorber, *Renew. Energy* 109 (2017) 49–65.
- [32] Q. Hu, Y. Li, Unsteady RANS simulations of Wells turbine under transient flow conditions, *J. Offshore Mech. Arct.* 140 (2018) 011901.
- [33] H. Chen, L. Qian, Z. Ma, W. Bai, Y. Li, D. Causon, C. Mingham, Application of an overset mesh based numerical wave tank for modelling realistic free-surface hydrodynamic problems, *Ocean Engineering* 176 (2019) 97–117.
- [34] R. A. Gingold, J. J. Monaghan, Smoothed particle hydrodynamics: theory and application to non-spherical stars, *Mon. Not. R. Astr. Soc.* 181 (1977) 375–389.
- [35] L. B. Lucy, A numerical approach to the testing of the fission hypothesis, *Astron. J.* 82 (1977) 1013.
- [36] A. Zhang, P. Sun, F. Ming, An SPH modeling of bubble rising and coalescing in three dimensions, *Comput. Methods Appl. Mech. Eng.* 294 (2015) 189–209.
- [37] C. Altomare, J. M. Domínguez, A. J. C. Crespo, J. González-Cao, T. Suzuki, M. Gómez-Gesteira, P. Troch, Long-crested wave generation and absorption for SPH-based DualSPHysics model, *Coast. Eng.* 127 (2017) 37–54.

- [38] C. Antoci, M. Gallati, S. Sibilla, Numerical simulation of fluid-structure interaction by SPH, *Comput. Struct.* 85 (2007) 879–890.
- [39] G. Oger, M. Doring, B. Alessandrini, O. Ferrant, Two-dimensional SPH simulations of wedge water entries, *J. Comput. Phys.* 213 (2006) 803–822.
- [40] K. Gong, H. Liu, B.-L. Wang, Water entry of a wedge based on SPH model with an improved boundary treatment, *J. Hydrodyn.* 21 (2009) 750–757.
- [41] S. Shao, Incompressible SPH simulation of water entry of a free-falling object, *Int. J. Numer. Methods Fluids* 59 (2009) 91–115.
- [42] G. Fourey, C. Hermange, D. L. Touzé, G. Oger, An efficient fsi coupling strategy between Smoothed Particle Hydrodynamics and Finite Element methods, *Comput. Phys. Commun.* 217 (2017) 66–81.
- [43] M. S. Shadloo, G. Oger, D. Le Touzé, Smoothed particle hydrodynamics method for fluid flows, towards industrial applications: Motivations, current state, and challenges, *Comput. Fluids* 136 (2016) 11–34.
- [44] A. J. C. Crespo, C. Altomare, J. M. Domínguez, J. González-Cao, M. Gómez-Gesteira, Towards simulating floating offshore oscillating water column converters with Smoothed Particle Hydrodynamics, *Coast. Eng.* 126 (2017) 11–26.
- [45] Z. Liu, Y. Wang, X. Hua, Numerical studies and proposal of design equations on cylindrical oscillating wave surge converters under regular waves using SPH, *Energy Convers. Manage.* 223 (2020) 112242.
- [46] M. Brito, R. B. Canelas, O. Garcá-Feal, J. M. Domínguez, A. J. C. Crespo, R. M. L. Ferreira, M. G. Neves, L. Teixeira, A numerical tool for modelling oscillating wave surge converter with nonlinear mechanical constraints, *Renew. Energy* 146 (2020) 2024–2043.
- [47] P. Ropero-Giralda, A. J. Crespo, B. Tagliafierro, C. Altomare, J. M. Domínguez, M. Gómez-Gesteira, G. Viccione, Efficiency and survivability analysis of a point-absorber wave energy converter using DualSPHysics, *Renew. Energy* 162 (2020) 1763–1776.
- [48] N. Quartier, A. J. C. Crespo, J. M. Domínguez, V. Stratigaki, P. Troch, Efficient response of an onshore Oscillating Water Column Wave Energy Converter using a one-phase SPH model coupled with a multiphysics library, *Appl. Ocean Res.* 115 (2021) 102856.

- [49] G. R. Liu, M. B. Liu, Smoothed Particle Hydrodynamics, World Scientific, 2003.
- [50] J. M. Domínguez, A. J. C. Crespo, M. Gómez-Gesteira, J. C. Marongiu, Neighbour lists in smoothed particle hydrodynamics, *Int. J. Numer. Methods Fluids* 67 (2011) 2026–2042.
- [51] H. Wendland, Piecewise polynomial, positive definite and compactly supported radial functions of minimal degree, *Adv. Comput. Math.* 4 (1995) 389–396.
- [52] J. J. Monaghan, Smoothed particle hydrodynamics, *Rep. Prog. Phys.* 68 (2005) 1703–1759.
- [53] A. J. C. Crespo, Users Guide for DualSPHysics code, <https://github.com/DualSPHysics/DualSPHysics/wiki> (2020).
- [54] J. J. Monaghan, A. Kocharyan, SPH simulation of multi-phase flow, *Comput. Phys. Commun.* 87 (1995) 225–235.
- [55] A. Colagrossi, M. Antuono, D. Le Touzé, Theoretical considerations on the free-surface role in the smoothed-particle-hydrodynamics model, *Phys. Rev. E* 79 (2009) 056701.
- [56] A. Colagrossi, M. Antuono, D. Le Touzé, Theoretical analysis and numerical verification of the consistency of viscous smoothed-particle-hydrodynamics formulations in simulating free-surface flows, *Phys. Rev. E* 84 (2011) 026705.
- [57] D. Molteni, A. Colagrossi, A simple procedure to improve the pressure evaluation in hydrodynamic context using the SPH, *Comput. Phys. Commun.* 180 (2009) 861–872.
- [58] M. Antuono, A. Colagrossi, S. Marrone, D. Molteni, Free-surface flows solved by means of SPH schemes with numerical diffusive terms, *Comput. Phys. Commun.* 181 (2010) 532–549.
- [59] J. J. Monaghan, Smoothed particle hydrodynamics, *Annu. Rev. Astron. Astrophys.* 30 (1992) 543–574.
- [60] M. S. Shadloo, R. Weiss, M. Yildiz, R. A. Dalrymple, Numerical simulation of long wave run-up for breaking and non-breaking waves, *Int. J. Offshore Polar* 25 (2015) 1–7.
- [61] J. J. Monaghan, K. A., Solitary waves on a cretan beach, *J. Waterway, Port, Coastal, Ocean Eng.* 125 (1999) 145–154.

- [62] S. J. Lind, R. Xu, P. K. Stansby, B. D. Rogers, Incompressible smoothed particle hydrodynamics for free-surface flows: A generalised diffusion-based algorithm for stability and validations for impulsive flows and propagating waves, *J. Comput. Phys.* 231 (2012) 1499–1523.
- [63] R. A. Dalrymple, O. Knio, SPH modelling of water waves, in: *Coastal Dynamics'01*, 2001, pp. 779–787.
- [64] A. J. C. Crespo, M. Gómez-Gesteira, R. A. Dalrymple, Boundary conditions generated by dynamic particles in SPH methods, *Comput. Mater. Contin.* 5 (2007) 173–184.
- [65] R. B. C. Canelas, A. J. C. Crespo, M. Brito, J. M. Domínguez, O. García-Feal, Extending DualSPHysics with a differential variational inequality: modeling fluid-mechanism interaction, *Appl. Ocean Res.* 76 (2018) 88–97.
- [66] O. S. Madsen, On the generation of long waves, *J. Geophys. Res.* 76 (1971) 8672–8683.
- [67] I. Zabala, J. Henriques, J. Blanco, A. Gomez, L. Gato, I. Bidaguren, A. Falcão, A. Amezaga, R. Gomes, Wave-induced real-fluid effects in marine energy converters: review and application to OWC devices, *Renew. Sustain. Energy Rev.* 111 (2019) 535–549.
- [68] S. Dai, S. Day, Z. Yuan, H. Wang, Investigation on the hydrodynamic scaling effect of an OWC type wave energy device using experiment and CFD simulation, *Renew. Energy* 142 (2019) 184–194.
- [69] A. Babarit, H. J. Todalshaug, On the maximum and actual capture width ratio of wave energy converters, in: *Proceedings of the 9th European Wave and Tidal Energy Conference*, 2011, pp. 1–18.
- [70] X. Garnaud, C. C. Mei, Comparison of wave power extraction by a compact array of small buoys and by a large buoy, in: *Proceedings of the 8th European Wave and Tidal Energy Conference*, 2009, pp. 934–942.
- [71] X. Garnaud, C. C. Mei, Wave-power extraction by a compact array of buoys, *J. Fluid Mech.* 635 (2009) 389–413.